Hetero-interface-engineered sulfur vacancy and oxygen doping in hollow Co_9S_8/Fe_7S_8 nanospheres towards monopersulfate activation for boosting intrinsic electron transfer in paracetamol degradation

Ta Cong Khiem [a], Nguyen Nhat Huy [b,c], Eilhann Kwon [d], Xiaoguang Duan [e], Stanisław Wacławek [f], Jorge Bedia [g], Yu-Chih Tsai [a], Afshin Ebrahimi [h,i], Farshid Ghanbari [j,*], Kun-Yi Andrew Lin [a,*]

[a] Department of Environmental Engineering & Innovation and Development Center of Sustainable Agriculture, National Chung Hsing University, Taichung 402, Taiwan
[b] Faculty of Environment and Natural Resources, Ho Chi Minh City University of Technology (HCMUT), Ho Chi Minh City 700000, Viet Nam
[c] Vietnam National University Ho Chi Minh City, Ho Chi Minh City 700000, Viet Nam
[d] Department of Earth Resources and Environmental Engineering, Hanyang University, SeongDong-Gu, Seoul, South Korea
[e] School of Chemical Engineering and Advanced Materials, The University of Adelaide, SA 5005, Australia
[f] Institute for Nanomaterials, Advanced Technologies and Innovation, Technical University of Liberec, Studentská 1402/2, 461 17 Liberec 1, Czech Republic
[g] Chemical Engineering Department, Facultad de Ciencias, Universidad Autonoma de Madrid, Campus Cantoblanco, Madrid E-28049, Spain
[h] Department of Environmental Health Engineering, School of Health, Isfahan University of Medical Sciences, Isfahan, Iran
[i] Environment Research Center, Research Institute for Primordial Prevention of Non-Communicable Disease, Isfahan University of Medical Sciences, Isfahan, Iran
[j] Research Center for Environmental Contaminants (RCEC), Abadan University of Medical Sciences, Abadan, Iran

ARTICLE INFO

ABSTRACT

Designing defects-rich hollow heterostructure bimetal sulfides is considered as an efficient strategy for accelerated monopersulfate (MPS) activation. Herein, mono-step sulfidation was employed to develop sulfur vacancy (SV)-rich hollow oxygen-doped Co_9S_8/Fe_7S_8 (O-CSFS). SV and oxygen doping-induced highly electroactive sites, low charge resistance, and increased conductivity of O-CSFS accounted for its superior performance. Reactive oxygen species (ROS)-driven pathway and electron transfer (ET)-driven pathway were revealed to be responsible for PCM degradation in O-CSFS/MPS system, but the role of ET-driven pathway was more significant. The ROS-driven pathway was mainly attributed to electrons-rich low valance of Co atoms which activated MPS to generate different ROS without $^\bullet OH$ contribution and with a greater role of $SO_4^{\bullet-}$ than $^1O_2$. Doped O, S species, and surface-active O-CSFS/MPS complex in ET-driven pathway, meanwhile, acquired electrons from PCM, resulting in enhanced PCM oxidation. This study provided more insight into ET-enhanced efficient PCM degradation induced by SV and oxygen-doping.

1. Introduction

As one of pharmaceuticals and personal care products (PPCPs), paracetamol (PCM) is widely used as an antipyretic and painkiller, allowing it to be found in wastewaters, and thereby raising potential concerns about ecology and human health due to its bioaccumulation and transformation to more toxic compounds [1]. To date, advanced oxidation processes (AOPs) have been developed and investigated intensively thanks to their promising potential for pollutant degradation based on the strong oxidizing capability of reactive species. Therefore, they have been adapted widely to degrade such PPCPs [2–7]. Take

Fenton/Fenton-like process as an example, the generation of $^\bullet OH$ and $O_2^{\bullet-}$ with a minor role was utilized to degrade 25 mg/L PCM within 60 min by $NiFe_2O_4$/F-doped g-Co_3N_4-activated H_2O_2 under visible-light with 1 g/L catalyst and 1 mL of H_2O_2 [8]. In another example, a new UV/Chlorine process developed by F Ghanbari et. al. was employed for PCM degradation. As a result, $Cl^\bullet/Cl_2^{\bullet-}$ and $^\bullet OH$ were revealed as the main species contributing to 85.3% of 0.1 mM PCM removal within 25 min with 0.5 mM Chlorine and an UV intensity of 1.43 mW/cm^2 [6]. In peracetic acid (PAA)/UVC-LED/Fe(II) AOP, 85.4% of 20 mg/L PCM was also found to degrade within 30 min with 3 mM PAA, 0.5 mM Fe(II), and UVC-LED at 254–258 nm due to the contribution of $^\bullet OH$ and R-O$^\bullet$ with

63.2% and ~21%, respectively [9]. Overall, PCM could be degraded but not totally, and high catalyst concentration and/or long time was required. Thus, it is essential to search for a promising strategy for more efficient PCM degradation. In this case, MPS activation would be a good alternative as it can generate $SO_4^{\bullet-}$ with a high redox potential of 2.5–3.1 V vs NHE [10]. In addition, various reactive oxygen species (ROS, e.g., $^{\bullet}OH$, $O_2^{\bullet-}$, and $^1O_2$), electron transfer (ET), and high-valent transition metal-oxo species with different oxidizing capabilities are usually generated. To achieve such an activation process, the biggest challenge is how to controllably tailor the way of generating ROS via radical mechanisms to nonradical ones driven by $^1O_2$, ET, or high-valent transition metal-oxo species. These nonradical pathways have been proven to have various features, such as capability of highly selective oxidation towards electrons-rich pollutants [11], pH-independent high oxidation efficiency [12], highly efficient utilization of oxidants [13], and adjustable oxidation potential by defective structures or elemental composition of the catalysts [14]. Nonetheless, the activation of MPS over metal-based catalysts in water via nonradical pathways is still limited by low stability of the catalysts due to poor exposed sites, low conductivity, and low surface area. To address these drawbacks, metal sulfides, especially cobalt-based sulfides (CS), have been developed recently [15–17]. Controllable electronic structure, low cost, and high conductivity are key advantages enabling CS to gain considerable interest. Moreover, increasing surface area is also deemed as one of the strategies to improve their activity. In this regard, cobalt glycerate (CoG) deserves consideration as it can be used as a template for fabrication of CS with high surface area. For example, Y. Zhao et. al. synthesized yolk-shell CoS spheres with high surface area by using CoG as a template and thioacetamide as S source. The resultant CoS exhibited a high specific capacitance of 632 F/g at 1 A/g [18]. However, lack of defects and active sites still prevents them from meeting expectations.

Defect engineering, an effective route, has been reported to be capable of modulating the redistribution of surface charge and maximizing the active sites owing to decrease in the number of coordination bonds [19]. In recent years, several methods have been adopted to introduce defects into metal sulfides to create more exposed active sites, such as heteroatom doping [20,21], heterointerface assembly [22,23], and changing surface oxidation property [24,25]. Among these, heterointerface assembly is becoming increasingly useful in view of its ability to regulate the electronic structure, thereby reconfiguring electrons of the heterostructure. Further, the central active sites of each individual component can be integrated to synergistically boost the reaction kinetics, which directly contribute to enhanced catalytic activity of the heterostructure. To take one example, CuS/NiS_2 nanoparticles with abundance of sulfur vacancy (SV) anchored on graphene designed by Z Wang et. al. exhibited a superior oxygen reduction reaction (ORR) performance with a high onset potential of 0.91 V vs. RHE and a half-wave potential of 0.77 V vs. RHE to other counterparts [26]. In another study, J Lin et. al. fabricated MoS_2/NiS_2 nanosheets on carbon cloth for overall water splitting. As a result, the obtained defect-enriched heterointerface afforded a low overpotential of 62 mV at 10 mA/cm^2 for alkaline hydrogen evolution reaction (alkaline HER) [27].

The heterostructures of cobalt-based metal sulfides can be composed of either the same metal, for example CoS/CoS_2 [28] and CoS/Co_9S_8 [29], or two different metals, such as CoS_2/NiS_2 [30] and Co_3S_4/ZnS [31]. Thanks to different redox potentials, which can enhance the synergistic effect via redox cycles, and thereby increasing the catalytic activity, the later has more advantage. Considering the low cost of Fe and the ability to efficiently activate MPS as reported in numerous studies, Fe-based sulfides (FS) could be a good choice for incorporation into CS. A recent study by H Xu showed that total degradation of antibiotics (ciprofloxacin and norfloxacin) could be achieved within 120 min with 0.6 g/L FeS and 6 mM MPS [32]. Fe_3S_4, Fe_7S_8, and FeS_2 prepared at different pH values using a facile hydrothermal treatment of $FeSO_4 \cdot 7$ H_2O and $Na_2S \cdot 9$ H_2O enabling removal of 93.6%, 63.2%, and 17.8% bisphenol A, respectively within 30 min with 50 mg/L catalysts and 0.5

mM MPS is another case in point [33].

Besides to modulating the electronic structure, surface oxidation property, and the conductivity of the electrocatalysts [34], oxygen doping can also create more active sites for subsequently boosted catalytic activity. The significantly heightened binding energy between the surface adsorbed oxygen species and the active sites contributing to enhanced oxygen evolution reaction (OER) induced by the introduction of oxygen into amorphous cobalt sulfide (C-S-O) as explored by Y Li et. al. [35] is a good example of this. Furthermore, Q Wu et. al. employed a facile hydro-solvothermal method to synthesize O-doped MoS_2 from thiourea and $Na_2MoO_4 \cdot 2$ H_2O. The as-prepared O-doped MoS_2 with abundance of defects endowed by oxygen doping and S_2^{2-} species, which was obtained at the optimal mole ratio of thiourea to $Na_2MoO_4 \cdot 2$ H_2O (40:1), presented a high current density of 24.11 mA/cm^2 at 200 mV vs. RHE for acidic HER [36]. With all the features that oxygen doping brings about, the role of oxygen in CS should not be dismissed. Therefore, it would be interesting to investigate how far heterointerface engineering-induced SV and oxygen doping in the CoG-derived CS/FS heterostructure can synergistically accelerate the MPS activation.

Herein, we report a mono-step sulfidation of hollow Fe-doped cobalt oxide (Fe-Co_3O_4), which was derived from nanocube-assembled hollow bimetallic cobalt-iron Prussian blue analogue (CoFePBA) nanospheres using CoG as a template via ion exchange reaction with $K_3[Fe(CN)_6]$ as Fe source, to construct hollow O-doped Co_9S_8/Fe_7S_8 heterostructure (O-CSFS) with enrichment of SV. Accordingly, such a unique heterostructure inheriting the synergistic effect of SV and oxygen doping was developed for the first time and employed for activation of MPS to degrade PCM. Low valence state of Co atoms with abundance of electrons enabled them to reduce MPS into different ROS, contributing to limited PCM degradation. The application of electrochemical analyses revealed that the surface-active O-CSFS/MPS complex formed from unreacted MPS and Co/Fe species in high valance states after first activation of MPS acquired electrons from undegraded PCM, resulting in enhanced PCM oxidation. At the same time, unreacted MPS accepted electrons mediated by O-CSFS to form more $SO_4^{\bullet-}$ and $^1O_2$, which further attacked PCM, leading to complete PCM degradation. Further X-ray photoelectron spectroscopy before and after reaction showed that doped oxygen along with S species also acted as electron acceptors, depriving electrons from PCM, and thereby facilitating the PCM degradation in ET-driven pathway. As a result, O-CSFS with enrichment of SV exhibited superior performance for MPS activation to degrade PCM completely within ~1.5 min with only 50 mg/L O-CSFS and 200 mg/L MPS. The findings of this study not only demonstrate the novel O-CSFS heterostructure with SV and oxygen doping increasing the conductivity, but also propose a promising route for efficient degradation of PPCPs.

2. Materials and methods

2.1. Catalyst preparation

2.1.1. Cobalt glycerate

All the chemicals used in this study were listed in Text S1. Firstly, cobalt glycerate (CoG) was prepared as follows. After the 150-mL autoclave containing 75 mL isopropanol and 1.5 mmol $Co(NO_3)_2 \cdot 6$ H_2O was stirred for 1 h, 24 mL glycerol was added while stirring for another 1 h before heating at 180 °C for 16 h. After that, CoG was collected by centrifugation, washing with ethanol (EtOH) before drying at 65 °C overnight.

2.1.2. Nanocube-assembled hollow CoFePBA-x nanospheres

After 250 mg CoG in 250 mL of 95% EtOH was sonicated for 15 min, 250 mL of 250 mg $K_3[Fe(CN)_6]$ in DI water was added and shaken thoroughly before letting stand for 6 h at room temperature, 50, and 70 °C. CoFePBA-x (x = r, 50, and 70 for those aged at room temperature, 50 and 70 °C, respectively) obtained after centrifugation, washing with EtOH, and drying at 65 °C overnight were carbonized at 350 °C (2 °C/
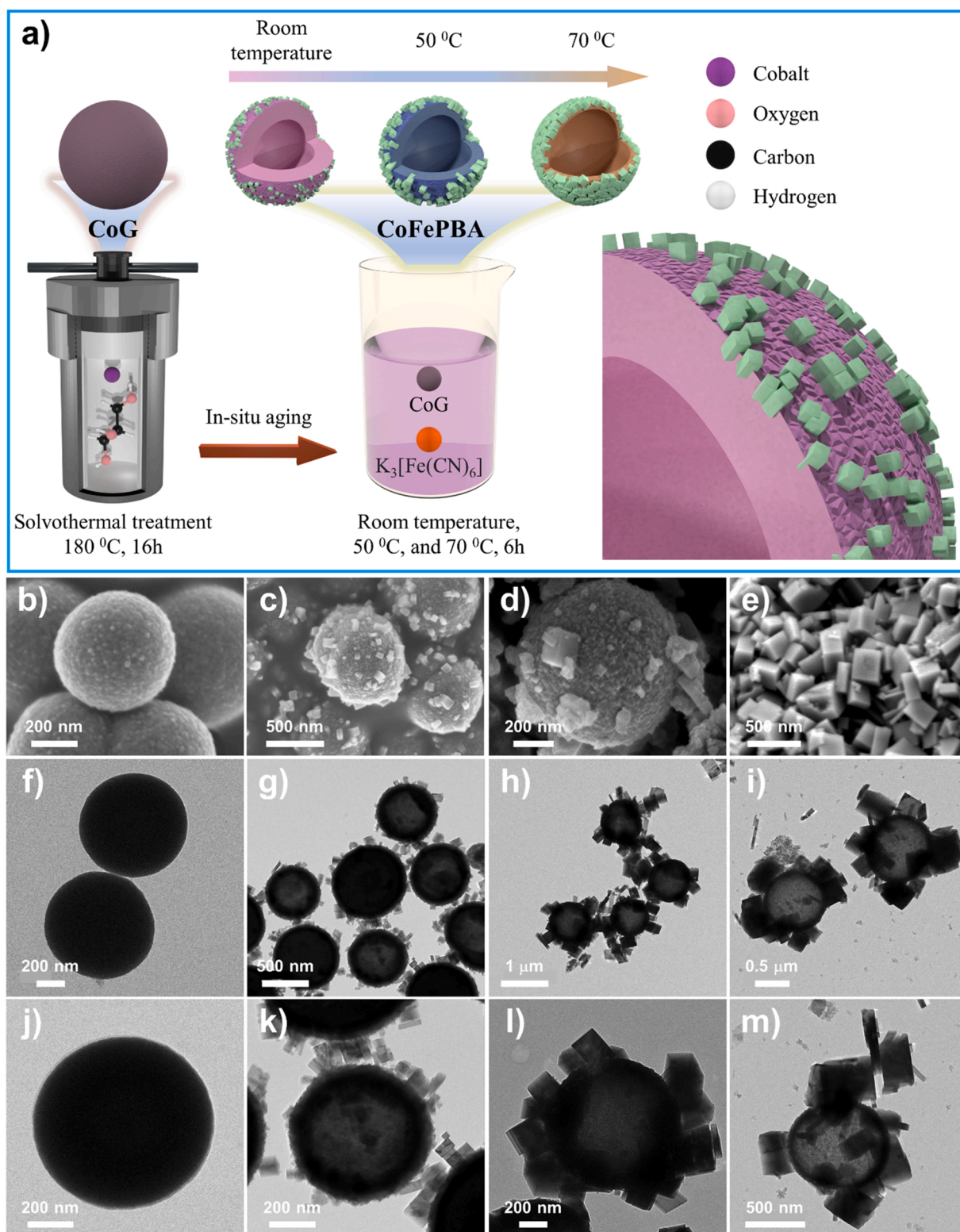
Fig. 1. (a) Schematic illustration of constructing nanocube-assembled hollow CoFePBA-x nanospheres; (b-e) SEM images of (b) CoG, (c) CoFePBA-r, (d) CoFePBA-50, and (e) CoFePBA-70; (f-m) TEM images of (f, j) CoG, (g, k) CoFePBA-r, (h, l) CoFePBA-50, and (i, m) CoFePBA-70.

min) for 2 h in N_2 to afford Co/CoFe/CoFe$_2$O$_4$ @C-x (CCFCF@C-x). Hereafter, the CCFCF@C-r was abbreviated to CCFCF@C.

1. O-doped Co$_9$S$_8$@Fe$_7$S$_8$

300 mg Fe-doped Co$_3$O$_4$ (Fe-Co$_3$O$_4$) obtained after calcining

CoFePBA-r at 400 °C for 2 h (2 °C/min) in the air was sonicated in an autoclave containing 60 mL of EtOH and 60 mL 0.3 M Na$_2$S·9 H$_2$O for 15 min before heating at 200 °C for 12 h. After finishing, the material collected by centrifugation, washing with EtOH, and drying at 65 °C overnight was carbonized at 350 °C (2 °C/min) for 2 h in N_2 to obtain hollow O-doped Co$_9$S$_8$ @Fe$_7$S$_8$ with SV (O-CSFS) nanospheres. To detect
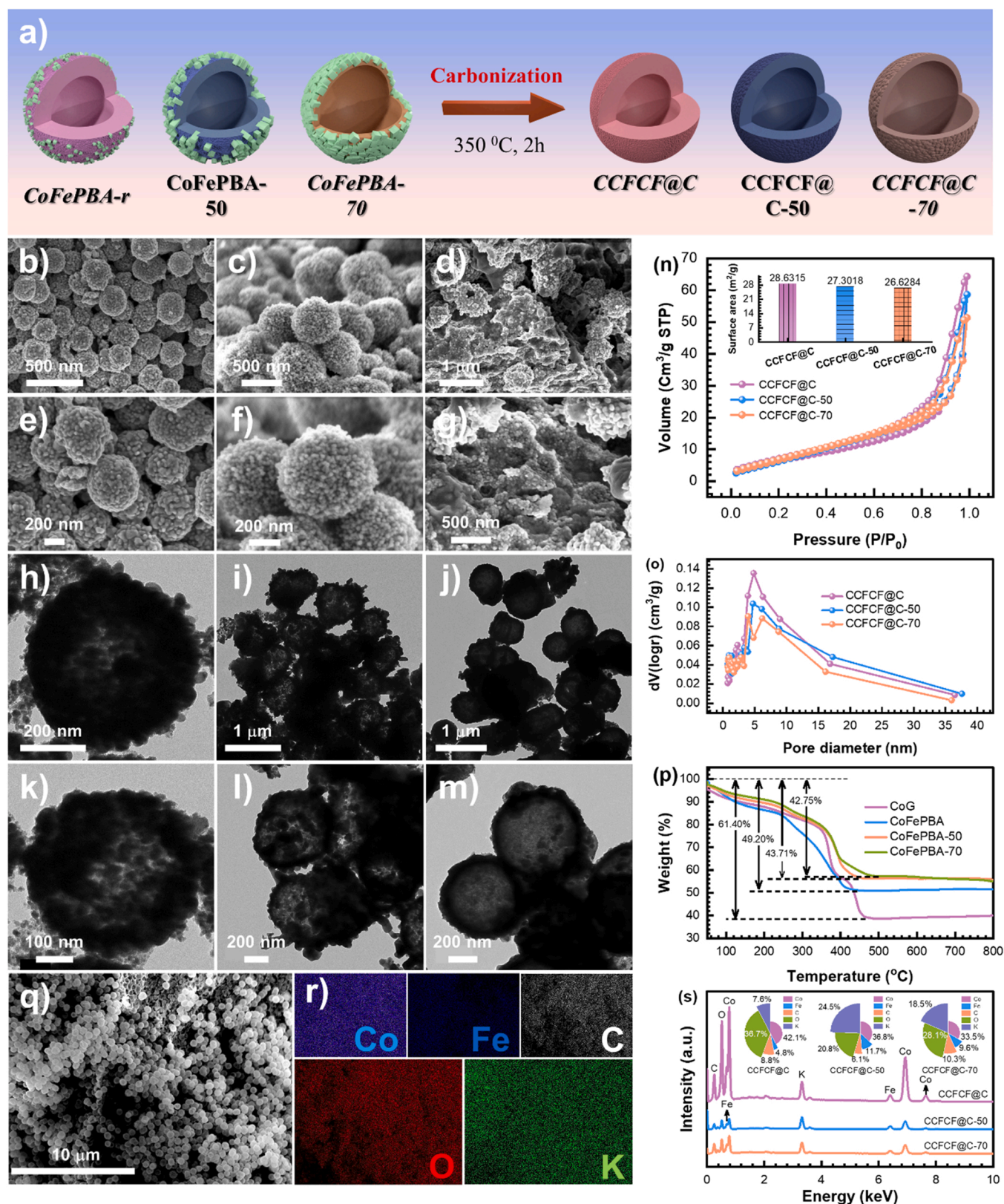
Fig. 2. (a) Schematic illustration of CCFCF@C-x composite preparation; (b-g) SEM and (h-m) TEM images of (b, e, h, k) CCFCF@C, (c, f, i, l) CCFCF@C-50, (d, g, j, m) CCFCF@C-70; (n) N₂-sorption isotherms and (o) pore size distribution of CCFCF@C-x; (p) TGA curves of CoFePBA-x; (q) SEM image and (r) associated EDS mapping of CCFCF@C; and (S) EDS spectra of CCFCF@C-x.

SV, Co$_9$S$_8$ was prepared using CoG as a template as follows. After the 150-mL autoclave containing 240 mg CoG and 360 mg thioacetamide dispersed in 120 mL of 95% EtOH was heated at 100 °C for 4 h, the product was centrifuged, washed with EtOH, and dry at 65 °C before carbonization at 350 °C for 2 h, 2 °C/min in N$_2$. After preparation, all the catalysts were characterized using methods provided in Text S2.

2.2. Electrochemical measurements

16 mg catalysts and 2 mg conductive carbon black were mixed with 0.8 mL of 1-methyl-2-pyrolidone and 0.2 mL of 10 g/L polyvinylidene fluoride as a binder under sonification for 1 h. The wight ratio of the above mixture was 8:1:1. After that, 10 µL of the above slurry was deposited on the glassy-carbon electrode (GCE, 0.3 cm in diameter, catalyst loading ~2.26 mg/cm^2) and dried at 65 °C for 30 min for using as working electrode, while Ag/AgCl and platinum wire were used as reference and counter electrode, respectively. All electrochemical tests were performed in 1 M KOH with Potentiostat (CHI 621D) after activating the electrode surface by using cyclic voltammetry (CV) at 10 mV/s in a potential range of 0.8274–1.6264 V vs. RHE for 4 cycles. The reversible hydrogen electrode (RHE) potential used here was obtained by converting the electrode potential according to the Nernst equation below.

$$E_{Vvs.RHE} = E_{Ag/AgCl} + 0.1976 + 0.0592 \times pH \tag{1}$$

The linear sweep voltammogram (LSV) was recorded at 5 mV/s from 1.4264 to 1.8264 V vs. RHE. For electrochemical impedance spectroscopy (EIS), the data was collected in a frequency range of 100 KHz to 0.01 Hz and amplitude of 5 mV.

To evaluate the electrochemically active surface area (ECSA, in cm^2), CV curves at different scan rates (20–100 mV/s) were performed in a non-faradic range of 1.1764–1.2764 V vs. RHE to obtain the double layer capacitance (C_{dl}, in F.cm^{-2} = mA.s.mV^{-1}.cm^{-2}), which is the slope of linear relationship between $\Delta j = (|J_a|+|J_c|)/2$ and scan rate (mV/s). The ECSA was then calculated according to Eq. (2).

$$ECSA = S.C_{dl}/C_s \tag{2}$$

where S is the working electrode area ($\pi \times 0.3^2/4$ cm^2), C_s is the specific capacitance obtained from an ideal electrode (usually 40×10^{-6} F.cm^{-2} in 1 M KOH).

The overpotential (V vs. RHE) was calculated according to Eq. (3):

$$\eta = E_{RHE} - 1.23 \tag{3}$$

2.3. Experimental procedures

The PCM degradation was conducted in a 100-mL glass beaker containing 50 mL of 20 mg/L PCM solution while stirring at 30 °C. To start the reaction, 5 mg each catalyst and 10 mg MPS (unless otherwise specified) were added. To evaluate effects of pH, the PCM solution was adjusted with HCl and NaOH before starting the reaction. Similarly, other affecting factors, including anions humic acid (HA) and scavengers (0.2–0.5 M TBA and MeOH, 0.2–0.5 mM NaN$_3$ and p-BQ) were also investigated. At regular intervals, 1.5 mL of the suspension was filtered through a 0.22 µM PVDF filter to a vial for analysis. The recyclability tests were also performed by reusing O-CSFS, but 50 mL of 20 mg/L PCM solution was increased to 1 L, and other conditions were kept. After each cycle, O-CSFS was collected by filtration, washed, and then dried at 65 °C. Benzoic acid (BA), 4-hydroxybenzoic acid (4-HBA), furfural alcohol (FFA), nitro blue tetrazolium chloride (NBT), and phenylmethyl sulfoxide (PMSO) were used probes to quantify •OH, SO$_4^{•-}$, ^{1}O$_2$, O$_2^{•-}$, and phenylmethyl sulfone (PMSO2), respectively, in which BA, 4-HBA, FFA, and PMSO/PMSO2 along with PCM were analyzed with a HPLC equipped with a UV detector and a C18 column. The detailed methods were presented in Text S3. In case effects of N$_2$ and O$_2$ were investigated, pure N$_2$/O$_2$ was bubbled directly into the beaker prior to experiments for

5 min. Meanwhile, NBT spectra were recorded with an UV-Vis spectrophotometer in a range of 200–700 nm. The concentration of MPS was analyzed with an UV-Vis spectrophotometer at 395 nm using KI [17,37], and the spectra were also recorded simultaneously (see more in Text S4).

2.4. ROS detection and ET test

Two spin reagents, including 5,5-dimethyl pyrroline oxide (DMPO) and 2,2,6,6- tetramethyl-4-piperidone (TEMP), were utilized to trap ROS in DI water (for •OH, SO$_4^{•-}$, and ^{1}O$_2$) and methanol (MeOH, for O$_2^{•-}$). The generated peaks characteristic of DMPO-•OH/SO$_4^{•-}$/O$_2^{•-}$ and TEMP-^{1}O$_2$ were detected with electron paramagnetic resonance (EPR) spectroscopy. In the case where PCM was concerned, DI water or part of MeOH was replaced with a curtained amount of PCM. See Text S5 for more detail. To examine ET of CCFCF@C and O-CFSS, MPS decomposition in the presence of PCM was first conducted at 30 °C using method in Text S4 to see if PCM accelerates the MPS decomposition. Second, electrochemical analyses like CV/LSV/i-t curves and open circuit potential (OCP) with and without MPS/PCM were performed in 0.5 M Na$_2$SO$_4$ with Potentiostat (CHI 621D) using procedures in Text S6.

3. Results and discussion

3.1. Construction of nanocube-assembled hollow CoFePBA-x nanospheres

Fig. 1(a) illustrates the preparation of nanocube-assembled hollow CoFePBA-x nanospheres from CoG as a template through ion exchange reaction with K$_3$[Fe(CN)$_6$] at room temperature, 50, and 70 °C for 6 h. During the reaction, Co^{2+} cations released from CoG gradually reacted with [Fe(CN)$_6$]$^{3-}$ to form CoFePBA nanocubes on the CoG surface. As the temperature increased, the Co^{2+} cations released more, allowing more CoFePBA nanocubes to be formed and the solid CoG, therefore, became hollower.

As CoG was utilized as a template for construction of nanocube-assembled hollow CoFePBA-x nanospheres, its surface morphology was examined by SEM and TEM images in Fig. 1(b, f, j). Monodispersed solid nanospheres with a diameter of ~ 600 nm can be seen. After reaction, the products in Fig. 1(c-e) were covered with CoFePBA nanocubes on the surface. TEM images in Fig. 1(g-i, k-m) reveal the hollow structure of these nanosphere. The higher the temperature, the hollower the structure and the more nanocubes on the surface. N$_2$ sorption isotherm and pore size distribution in Fig. S1 indicate these CoFePBA nanospheres possessed a higher surface area as well as a higher pore volume than the original CoG, in which the highest surface area and pore volume were found for CoFePBA-r. Compared with CoFePBA-50, a much decrease in surface area of CoFePBA-70 suggests room temperature was the most favorable. Combined with changes of functional groups in FTIR spectra (Fig. S2), CoG was successfully transformed into hollow CoFePBA-x, which are expected to be a good precursor for subsequent fabrication of efficient catalysts.

3.2. Nanocube-assembled hollow CoFePBA nanospheres-derived CCFCF@C-x composites

The CCFCF@C-x composites were synthesized by carbonization of nanocube-assembled hollow CoFePBA-x nanospheres in N$_2$ (Fig. 2a). The surface morphology of these composites is exhibited in Fig. 2(b-g), in which CCFCF@C and CCFCF@C-50 still remained the sphere, but most of CCFCF@C-70 was deformed, largely because of the melting of CoFePBA-70 at high temperature. TEM images in Fig. 2(h-m) confirmed this. While CCFCF@C was mainly porous and hollow spheres with uniform nanoparticles on the outer surface, CCFCF@C-50 melted partly, thereby limiting its cavity inside. The highest degree of melting was found for CCFCF@C-70 as most of its cavity was sealed. Thus, CCFCF@C was likely to possess the highest surface area as well as the highest pore volume. To confirm this, BET measurement was performed. As Fig. 2(n)
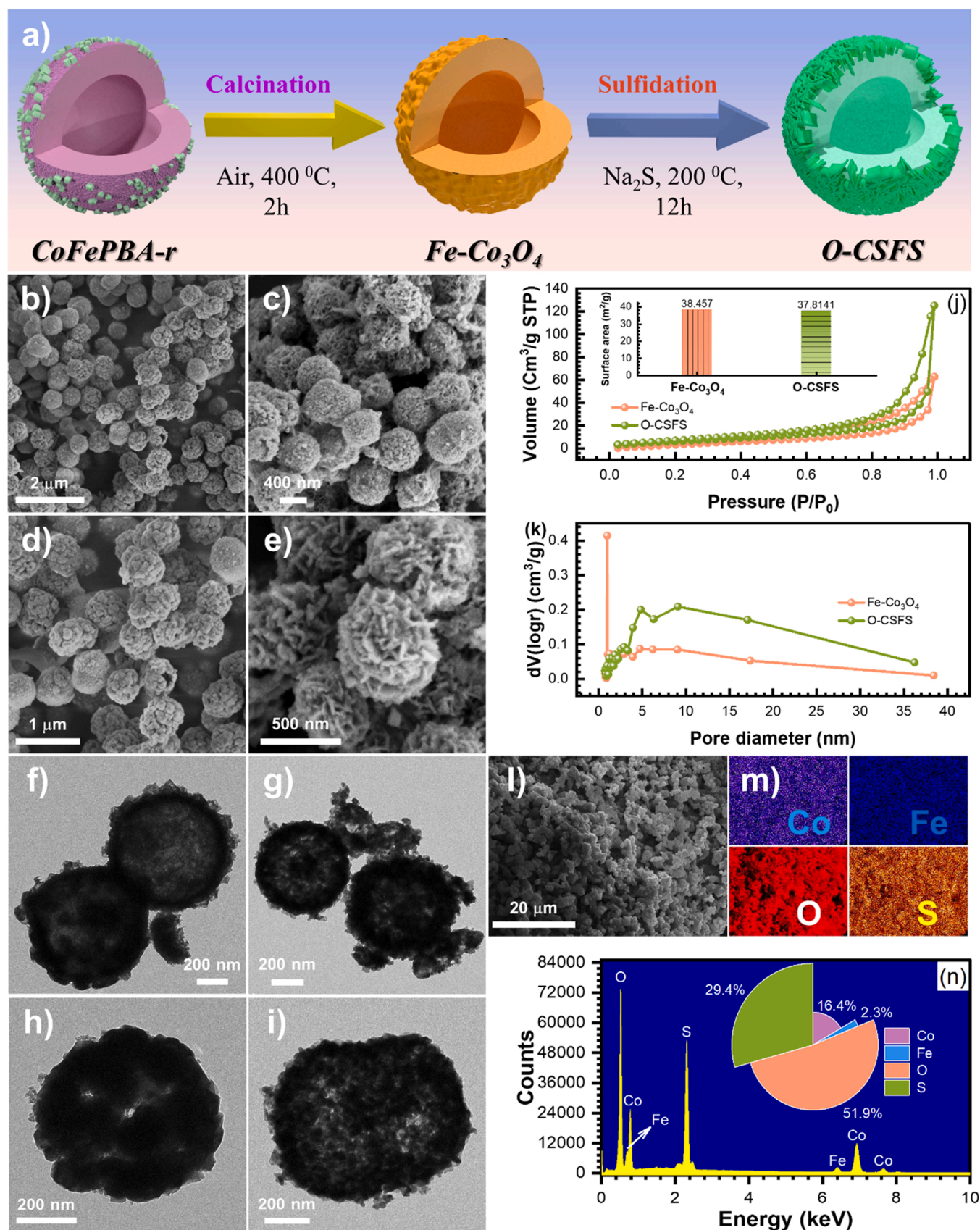
Fig. 3. (a) Schematic illustration of O-CSFS preparation; (b-e) SEM and (f-i) TEM images of (b, d, f, h) Fe-Co$_3$O$_4$, (c, e, g, i) O-CSFS; (j) N$_2$-sorption isotherms and (k) pore size distribution of Fe-Co$_3$O$_4$ and O-CSFS; (l) SEM image and (m) associated EDS mapping of O-CSFS; and (n) EDS spectra of O-CSFS.
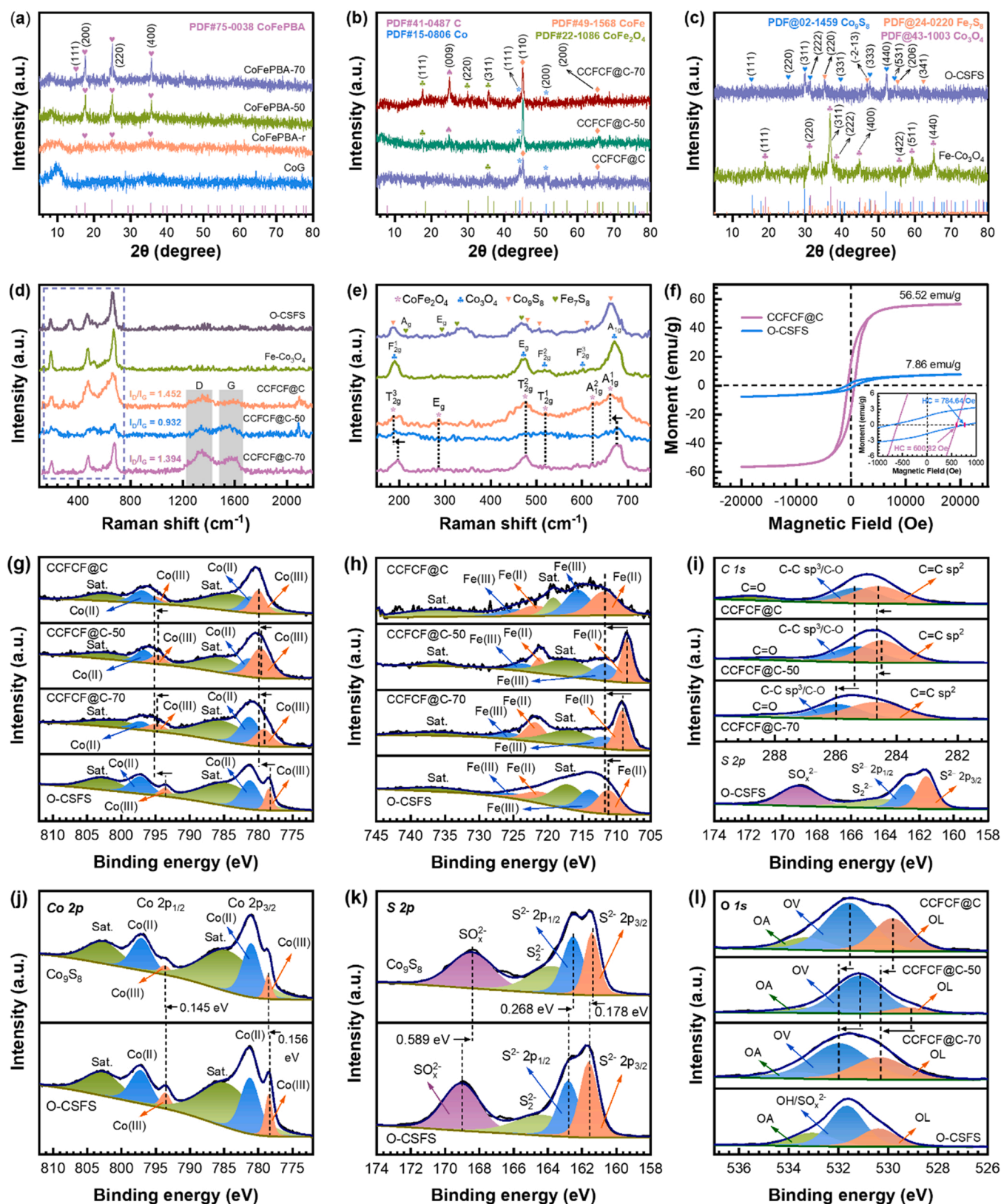
Fig. 4. (a-c) XRD patterns of (a) CoG and CoFePBA-x, (b) CCFCF@C-x, (c) Fe-Co₃O₄ and O-CSFS; (d, e) Raman spectra of CCFCF@C-x, Fe-Co₃O₄, and O-CSFS; (f) Magnetic hysteresis loops of CCFCF@C and O-CSFS; (g-i, l) XPS spectra of CCFCF@C-x and O-CSFS: (g) Co *2p*, (h) Fe *2p*, (i) C *1 s* and S *2p*, and (j) O *1 s*; and (j, k) XPS spectra of Co₉S₈ and O-CSFS: (j) Co *2p* and (k) S *2p*.

shows, the highest amount of N_2 absorbed was observed for CCFCF@C, while the lowest was for CCFCF@C-70. This subsequently led to the highest surface area of CCFCF@C as shown in the inset of Fig. 2(n). In line with N_2 sorption isotherm, pore size distribution in Fig. 2(o) also displayed the highest pore volume over a large pore diameter range of CCFCF@C. Overall, high surface area and pore volume may contribute to higher activity. The thermal stability of CoG after reaction was investigated by thermogravimetric analysis (TGA) in Fig. 2(p). The results indicate the introduction of Fe reduced the weight loss. Among CoFePBA-x, CoFePBA-70 was the most stable.

EDS mapping in Fig. 2(r) showed the uniform distribution of five elements (Co, Fe, C, O, and K) over a selected area in Fig. 2(q), suggesting the existence of these elements in CCFCF@C. K in this case was just considered as an impurity. EDS spectra in Fig. 2(s) further confirmed this with differences in elemental contents and peak intensity between CCFCF@C-x.

3.3. Conversion into O-CSFS

The preparation of O-CSFS is illustrated in Fig. 3(a). CoFePBA-r was first oxidized to Fe-Co_3O_4 for conversion into O-CSFS by sulfidation with Na_2S. SEM images in Fig. 3(b, c, e, f) reveal the difference in surface morphology between Fe-Co_3O_4 and O-CSFS. Hollow spheres with rounded nanoparticles on the outer surface of Fe-Co_3O_4 was observed. Meanwhile, the surface of O-CSFS was more porous, demonstrating the sulfidation process took effect. TEM images in Fig. 3(d, e, g, h) show the hollow configuration of these two materials, suggesting the sulfidation did not destroy the morphology but rather remained the original hollow structure of Fe-Co_3O_4. Considering surface area and pore volume, Fig. 3 (j, k) show surface area decreased slightly after sulfidation as 37.8141 m^2/g for O-CSFS was lower than 38.457 m^2/g for Fe-Co_3O_4. However, the pore volume of O-CSFS was higher as displayed in Fig. 3(k) (see more in Table S1). EDS mapping of O-CSFS in Fig. 3(m) exhibits the uniform distribution of Co, Fe, O, and S over a selected area in Fig. 3(l). The EDS spectrum in Fig. 3(n) shows the presence of these four elements, especially O which suggests the sulfidation was favorable for oxygen doping.

3.4. Crystallography

XRD patterns of CoG and i.e., CoFePBA-x were displayed in Fig. 4(a). For CoG, there was no noticeable peaks in the pattern, revealing that the crystal of CoG was just amorphous. For CoFePBA-x, three noticeable peaks at 17.58, 24.97 and 30.70° were well indexed to (200), (220) and (222) planes, respectively of CoFePBA (PDF#75–0038). Compared with CoFePBA-r, these peaks of CoFePBA-50 and CoFePBA-70 were higher and sharper, indicating that increase in the aging temperature was more conducive to the formation of CoFePBA, but in general, CoG was successfully transformed into CoFePBA.

As CCFCF@C-x were obtained from CoFePBA-x, their XRD patterns were shown in Fig. 4(b). In these samples, the presence of diffraction peak at ~44.18° was assigned to the (111) plane of Co (PDF#15–0806), implying that Co(II) was reduced to Co during the carbonization process. In addition, the highest peak at ∼ 44.97°, which was typical for the reflection of bimetallic CoFe alloy (PDF#49–1568), indicated the existence of CoFe in these carbonized products. Three peaks at 18.32, 30.14, and 35.50° in the CCFCF@C-70 sample, on the other hand, were characteristic of (111), (220), and (311) planes, respectively of $CoFe_2O_4$ (PDF#22–1086). Compared with CCFCF@C-70, one diffraction peak at 18.32° for CCFCF@C-50 and at 35.50° for CCFCF@C suggested the presence of $CoFe_2O_4$ in these two samples. As CoFePBA-x were employed as precursors, C is expected to be existed in the resultant samples. The characteristic peak at ~15.88° in CCFCF@C-50 and CCFCF@C-70, which was ascribed to the (006) plane of graphitic carbon (PDF#41–0487), demonstrated this. However, this peak in CCFCF@C was quite low, indicating the presence of carbon with low amount in the

Table 1

D-spacings (Å)[a] of Co_9S_8 and O-CSFS.

Crystal plane	Co_9S_8	O-CSFS
(111)	5.6606	5.6389
(311)	2.9668	2.9885
(222)	2.8474	2.8859
(333)	1.8986	1.9176
(440)	1.7440	1.7498

[a] Calculated from XRD using Eq. (5)

$$d = n\lambda/(2\sin\theta) \tag{5}$$

CCFCF@C sample.

In addition to carbonization, CoFePBA-r was also calcinated in the air to afford Fe-Co_3O_4 and subsequent conversion into O-CSFS. The XRD patterns of these two materials were compared in Fig. 4(c). For Fe-Co_3O_4, seven diffraction peaks at 19.04, 31.35, 36.94, 38.64, 44.92, 59.51, and 65.41° were well indexed to the (111), (220), (311), (222), (400), (511), and (440) planes, respectively of Co_3O_4 (PDF#43–1003). Besides, there was no peaks typical of the existence of Fe, suggesting that Fe just played as a dopant because of its low amount resulted from the ion exchange reaction with $[Fe(CN)_6]^{3-}$ anions. After sulfidation, the characteristic peaks in the Fe-Co_3O_4 sample disappeared, while new peaks evolved. Among these, eight diffraction peaks at 15.25, 25.34, 29.94, 31.32, 39.69, 47.72, 52.25, and 54.39° were found to match well the (111), (220), (311), (222), (331), (333), (440), and (531) planes, respectively of Co_9S_8 (PDF#02–1459). Other four peaks at 35.36, 49.93, 55.20, and 62.32°, in contrast, corresponded to the (220), (−2 to 13), (206), and (341) planes of Fe_7S_8 (PDF#24–0220). These results suggests that the sulfidation converted Fe-Co_3O_4 into bimetal sulfides composed of Co_9S_8 and Fe_7S_8. To know the effect of Fe incorporation and sulfidation on the crystal structure of O-CSFS, XRD patterns of O-CSFS and Co_9S_8 were compared together. It is apparent from Fig. S3 that all peaks of O-CSFS was significantly weaker and wider than those of Co_9S_8, implying poorer crystallinity of CSFS [19]. Upward movement to higher angle, on the other hand, was found for all the planes of O-CSFS, especially (311) and (440) (Fig. S3(b, c)), suggesting O-CSFS had larger D-spacings (Table 1). Further, O-CSFS also had much higher microstrain of 1.4960% than Co_9S_8 (0.883%, calculated from XRD using Eq. (4)). Thus, the results reveal the possible existence of defects induced by SV in O-CSFS.

$$\varepsilon = 100 * \beta/(4\tan\theta) \tag{4}$$

where ε is microstrain (%); β is the line broadening at full width at half maximum (FWHM) in radian, and θ is Bragg's angle (radian). where d is D-spacing (Å); n is diffraction order, n = 1; λ is x-ray wavelength with Cuk$_\alpha$ radiation, λ = 1.5406 Å; and θ is Bragg's angle (radian).

3.5. Raman spectra and magnetic property

The structural evolution of these catalysts can be verified by Raman spectra. Fig. 4(d) shows two spectral ranges below and above 800 cm^{-1} in CCFCF@C-x, and only one range below 800 cm^{-1} in Fe-Co_3O_4 and O-CSFS. Several bands below 800 cm^{-1} were characteristic of metal-based components (Fig. 4(e)), while two pronounced bands above 800 cm^{-1} in CCFCF@C-x indicated the existence of carbon.

Those at 1341.98–1352.43 and 1561.38–1588.81 cm^{-1} were typical of disordered (D-band) and graphitic (G-band) carbons, respectively. Compared to other CCFCF@C-x, CCFCF@C had the highest intensity ratio (I_D/I_G) of 1.452, while the lowest was observed for CCFCF@C-50 (at 0.932), indicating the highest defect and graphitization degrees in CCFCF@C and CCFCF@C-50, respectively. Thus, CCFCF@C had the largest carbon defect content, which subsequently could contribute to improved catalytic performance. In the range below 800 cm^{-1}, all
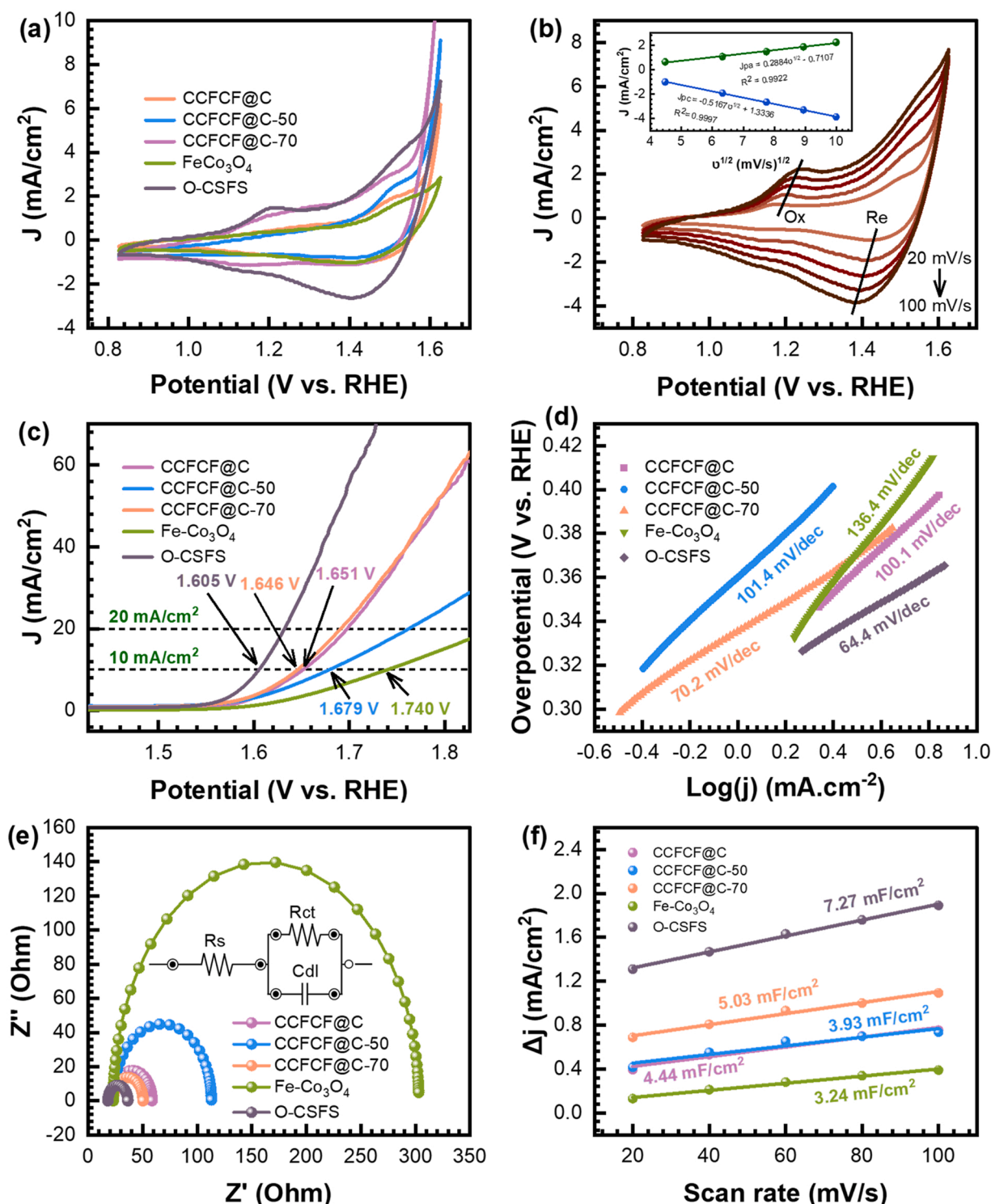
Fig. 5. (a) CV curves of CCFCF@C-x, Fe-Co$_3$O$_4$, and O-CSFS; (b) CV curve of O-CSFS at different scan rates (inset is correlation of J vs. $\upsilon^{1/2}$); (c) LSV curves, (d) Tafel plots, (e) EIS (inset is equivalent circuit model), and (f) C$_{dl}$ values obtained from current density vs scan rate of CCFCF@C-x, Fe-Co$_3$O$_4$, and O-CSFS.

CCFCF@C-x exhibited five typical peaks, including three T$_{2\,g}$ modes (187.06–196.39, ~477.24, ~519.77 cm^{-1}), one E$_g$ mode (~286.57 cm^{-1}), and two A$_{1\,g}$ modes (~623.63, 661.69–676.37 cm^{-1}) in the spinel structure of CoFe$_2$O$_4$. It is reported that A$_{1\,g}$ and T$_{2\,g}$ modes were associated with the symmetric stretching and asymmetric stretching of oxygen atoms, respectively with regard to tetrahedral (Co) and octahedral (Fe atoms) sites, while E$_g$ mode belonged to the symmetric bending of Co(Fe)-O bond [38]. These results revealed the existence of CoFe$_2$O$_4$ in CCFCF@C-x. Meanwhile, there was no peak typical

of Co or CoFe alloy, largely due to the absence of molecular vibration caused by pure metal in the Raman spectra [39]. Considering the position, T$_{2g}^3$ and A$_{1g}^1$ peaks shifted up as increasing temperature during the construction of CoFePBA-x. In addition, these peaks in CCFF@C and CCFCF@C-50 were broader and weaker than those in CCFCF@C-70, implying higher defect content was exposed in both CCFCF@C and CCFCF@C-50. This defect later would greatly facilitate the movement of oxygen and subsequently the formation of oxygen vacancy (OV) due to

weak molecular bond. OV is believed to be capable of capturing oxygen atoms from oxidants, creating more active species and accelerating catalytic reactions [37].

In Fe-Co$_3$O$_4$, five peaks at 190, 475, 517.79, 602.11, and 671.02 cm^{-1} were detected, probably be typified by F$_{2g}^1$, E$_g$, F$_{2g}^2$, F$_{2g}^3$, and A$_{1g}$ modes of Co$_3$O$_4$, respectively. The E$_g$ mode was associated with tetrahedral site (CoO$_4$) and the A$_{1g}$ mode was associated with octahedral site (CoO$_6$). After sulfidation, these characteristic peaks were changed. The first five peaks at 186.44, 479.98, 506.22, 609.83, and 662.94 cm^{-1} were assigned to Co$_9$S$_8$ [40], whereas the second four peaks at 214.55, 292.79, 326.12, and 467.29 cm^{-1} indicated the presence of Fe$_7$S$_8$. Among those peaks of Fe$_7$S$_8$, the two peaks at 214.55, 292.79 cm^{-1} were representative of out-plane (A$_g$) and in-plane (E$_g$) phonon modes of Fe-S in Fe$_7$S$_8$ [41]. Overall, O-CSFS was a composite composed of Co$_9$S$_8$ and Fe$_7$S$_8$.

Magnetization of CCFCF@C and O-CSFS is shown in Fig. 4(f). Clearly, the saturation magnetization (Ms) of 56.52 emu/g was observed in CCFCF@C, much higher than that in O-CSFS. However, O-CSFS had a higher coercivity (H$_C$) value of 784.64 Oe than CCFCF@C (600.82 Oe), suggesting O-CSFS was magnetically harder. The magnetism in CCFCF@C reveals metal species were in lower oxidation states, which is believed to enhance the catalytic activity. O-CSFS, on the other hand, had the magnetism because of Fe$_7$S$_8$ [42].

3.6. Surface chemical analysis

From full XPS spectra in Fig. S4, four elements (Co, Fe, C, and O) in CCFCF@C-x and four elements (Co, Fe, O, and S) in O-CSFS were displayed, suggesting that these elements comprised these two catalysts. Further, the presence of O in O-CSFS indicates that oxygen was doped to the bimetal sulfides, which was also confirmed by EDS and elemental mapping in Fig. 3(m, n).

For Co 2p, Fig. 4(g) shows two obviously high peaks at ~780 and ~796 eV in CCFCF@C-x, which were attributed to Co 2p$_{3/2}$ and Co 2p$_{1/2}$. Each of them was composed of two components (Co(II) and Co(III)) at high and low binding energies, respectively. As x increased from room temperature to 70 ^{0}C, the peak position of Co(III) underwent blue-shifts of 0.84 eV in CCFCF@C-70 compared to that in CCFCF@C, disclosing that the introduction of Fe via ion exchange reaction changed the binding locality near Co atoms. Two peaks characteristic of Co 2p$_{3/2}$ and Co 2p$_{1/2}$ in O-CSFS were also observed, but the deconvolution of these two peaks into two pairs of Co(II) and Co(III) was more obvious. Furthermore, both CCFCF@C and O-CSFS were derived from the same precursor (i.e., CoFePBA-r), but Co(III) in O-CSFS situated at much lower binding energy than that in CCFCF@C and even lower than that in CCFCF@C-70, implying that the sulfidation was more favorable for changing the electronic structure of a certain catalyst. As a result, Co(II) content in O-CSFS was the highest (Fig. S5, calculated from Table S2), partly accounting for enhanced activity of O-CSFS. The same phenomenon was also seen for Fe 2p (Fig. 4(h)). However, the downshift in Fe(II) of CCFCF@C-50 and CCFCF@C-70 was more notable, and thereby resulting in high Fe(II) content (Fig. S5, calculated from Table S3).

Fig. 4(i) shows XPS spectra of C 1s in CCFCF@C-x and S 2p in O-CSFS. Overall, three peaks corresponding to C=O, C-C sp^3/C-O, and C-C sp^2 were seen in C 1s spectra of CCFCF@C-x [43,44], while four peaks at 161.60, 162.80, 164.32, and 169.00 eV, belonged to S^{2-} 2p$_{3/2}$, S^{2-} 2p$_{1/2}$, S$_2^{2-}$, and SO$_x^{2-}$ [17,45], were detected in S 2p spectrum of O-CSFS. It is known that carbon defects in C=O or C-O species and high conductivity in C=C species could accelerate the catalytic activity [46]. Thus, C species in CCFCF@C-x could be responsible for varying activities. Negative shift in binding energy of Co 2p and Fe 2p of O-CSFS compared to those of CCFCF@C occurred although both of them were derived from the same precursor. Therefore, O-CSFS might have lattice defects after sulfidation. To clear this up, XPS spectra of O-CSFS in comparison with those of Co$_9$S$_8$ is needed. Fig. 4(j) depicts the backward movement of Co

(III) 2p$_{1/2}$ and Co(III) 2p$_{3/2}$ by 0.145 and 0.156 eV compared to those of Co$_9$S$_8$, respectively. In other words, the coordinative locality of those sites occupied by Co(III) was changed, resulting in increased electron density of Co and lowered oxidation state of Co, sustaining that Fe incorporation caused a significant redistribution of electron density on Co sites. Due to weak coordination in the crystal, or rather the unpaired electron richness of unbound metal species, lattice defects could boost the activity of defects-enriched catalysts [17]. In metal sulfides, the lattice defects could be associated with SV (a type of the most common anion defects). As Fig. 4(k) shows, although S 2p of both Co$_9$S$_8$ and O-CSFS was observed to have four characteristic peaks, corresponding to S^{2-} doublets, S$_2^{2-}$, and SO$_x^{2-}$, S^{2-} 2p$_{3/2}$ and S^{2-} 2p$_{1/2}$ in the S^{2-} doublets as well as SO$_x^{2-}$ of O-CSFS shifted positively by 0.178, 0.268, and 0.589 eV, respectively, indicating SV had great influence on the electronic structure of S 2p, increasing partly positive charge of S$^{\delta+}$ [20]. At the same time, the electron density of S sites in O-CSFS decreased [22], which can facilitate the acceptance of electrons from pollutants by S sites, tailoring the degradation to ET-driven nonradical pathway. From XRD and XPS, the incorporation of Fe into Co$_9$S$_8$ exerted great influence on the electronic structure of O-CSFS by inducing SV.

For O 1s, three characteristic peaks can be seen in Fig. 4(l), which were known as lattice oxygen (OL), OV, and absorbed oxygen (OA) for CCFCF@C-x and OL, -OH/SO$_x^{2-}$, and OA for O-CSFS. Compared to those of CCFCF@C-x, oxygen peaks of CCFCF@ −50 situated at the lowest binding energies as against those of CCFCF@C-70. In addition, the relative OV in CCFCF@ −50 was also the highest, while the lowest was for OL, which was indicated clearly by the highest ratio of OV/(OA+OL) of CCFCF@C-50 in Fig. S5 (obtained from Table S4). Due to abundance of OV, oxygen in CCFCF@C-50 mainly existed on the surface, which was deemed as the active site for accelerating the catalytic performance [37]. Therefore, the enhanced activity of CCFCF@ −50, if possible, could be owing to its highest OV content. As regards oxygen in O-CSFS, the appearance of OL reveals that oxygen had a certain chemical bond with metals after sulfidation. OH/SO$_x^{2-}$, on the other hand, suggest that OH and SO$_x^{2-}$ groups were formed after exposing to the air. Finally, the detection of OA could be due to physicochemical adsorption of water on the surface of O-CSFS [34].

3.7. Electrochemical performance

The CV curves of as-prepared catalysts performed at 60 mV/s in a potential window range of 0.8274–1.6264 V vs. RHE were depicted in Fig. 5(a). Several reversible redox peaks with difference in the current density were observed on the electrodes coated with these catalysts. The lowest peak current density was seen for GCE coated with Fe-Co$_3$O$_4$ (Fe-Co$_3$O$_4$/GCE), while an obvious increase in the redox peak current density occurred when O-CSFS was applied, indicating the inferior ET of Fe-Co$_3$O$_4$ (possibly because of less active sites) and the enhanced interfacial redox property of O-CSFS. Compared with O-CSFS, the surface area of Fe-Co$_3$O$_4$ was higher but its lower redox property suggests that the good conductivity of O-CSFS, largely resulted from the synergetic effect of bimetal sulfides as well as the incorporation of SV and oxygen doping. On the other hand, the peak current density of CCFCF@C/GCE followed the order of CCFCF@C-50/GCE < CCFCF@C/GCE < CCFCF@C-70/ GCE, closely accorded with the highest I$_D$/I$_G$ of CCFCF@C and CCFCF@C-70, while the lowest I$_D$/I$_G$ of CCFCF@C-50, implying the determining role of carbon defects in dominating the redox property of these three catalysts. In addition, high Co(II) content of CCFCF@C and CCFCF@C-70 could also account for their higher electrochemical performance.

CV curves at different scan rates from 20 mV/s to 100 mV/s were also recorded. As the scan rate increased, the peak current density of both anodic and cathodic peaks was significantly enhanced for all the coated electrodes (Fig. 5(b) and Fig. S6). The relationship between square root of the scan rate and the redox peak current density was then found to be linear as shown in the inset of Fig. 5(b) and Fig. S7, from
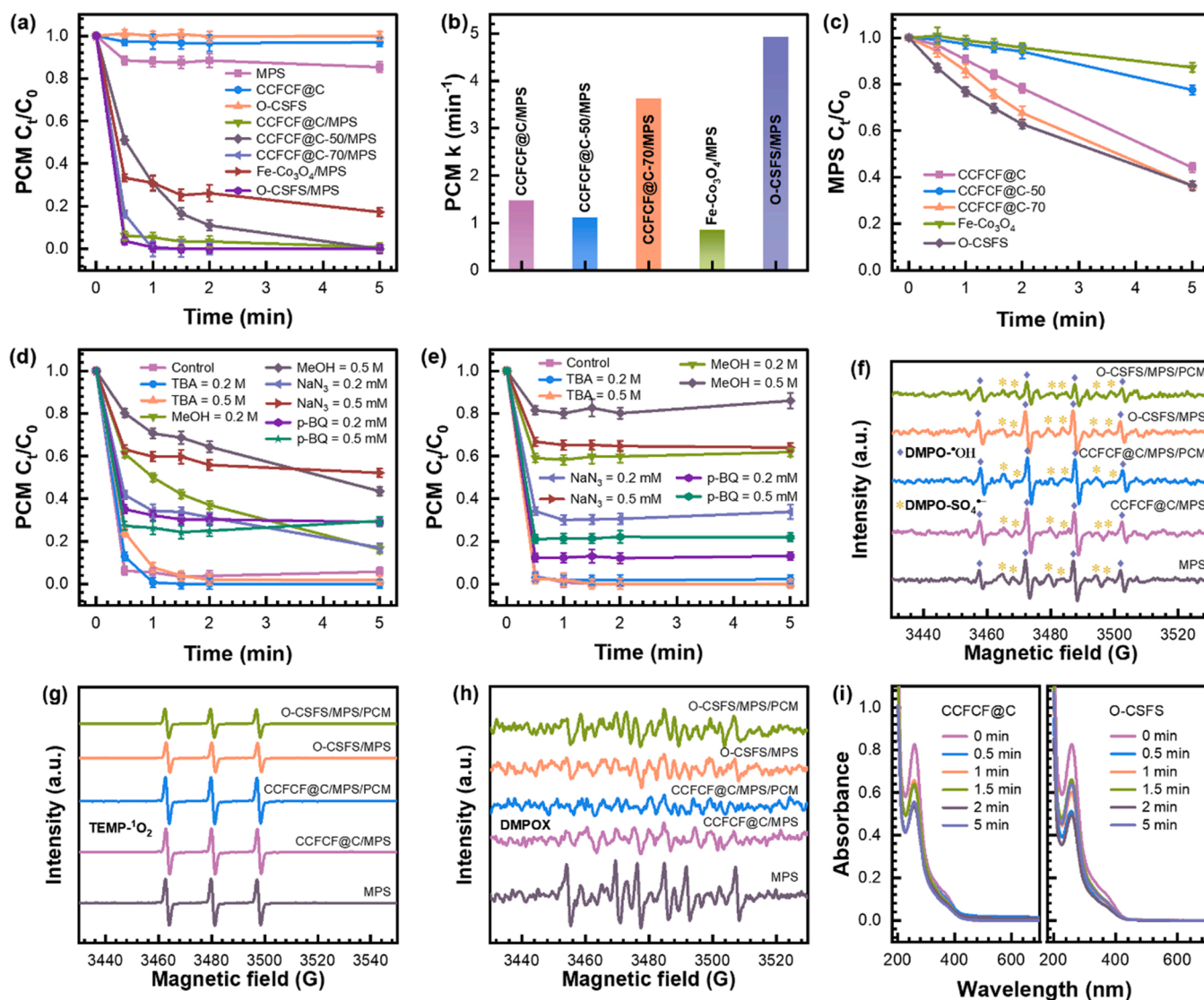
Fig. 6. (a) A comparison of MPS activation for PCM degradation over different catalysts (catalysts = 100 mg/L, MPS = 200 mg/L, PCM = 20 mg/L, initial pH = 6.6, and t = 30 ^{0}C); (b) corresponding first order reaction rate (k, in min^{-1}); (c) MPS decomposition; (d, e) PCM degradation profiles of (d) CCFCF@C and (e) O-CSFS in the presence of different scavengers (catalysts = 100 mg/L, MPS = 200 mg/L, PCM = 20 mg/L, initial pH = 6.6, and t = 30 ^{0}C); (f-h) EPR spectra of (e) DMPO-$^{\bullet}$OH/SO$_4^{\bullet-}$ in DI water, (g) TEMP-^{1}O$_2$ in DI water, and (h) DMPOX in MeOH [catalysts = 100 mg/L, MPS = 200 mg/L, PCM = 20 mg/L, DMPO = TEMP = 3 g/L, solvent = DI water (c, e), solvent = MeOH (d)]; and (i) UV–vis spectra of NBT reduction over CCFCF@C and O-CSFS (catalysts = 100 mg/L, MPS = 200 mg/L, NBT = 60 mg/L, and t = 30 °C).

which the absorption-controlled behavior of these catalysts could be deduced. In contrast, there was only one reduction peak in the CV curve of CCFCF@C-50/GCE, whose peak current density had a linear relationship with square root of the scan rate ($J_{pc} = -0.1686\sqrt{v} + 0.4764$, R^2 = 0.9908), suggesting the diffusion-controlled behavior of CCFCF@C-50 [47]. In addition, it is observed from the slope of the above regression equations (J_{pa}) that the highest slope value was seen for O-CSFS/GCE, indicating the greatest diffusion coefficient and hence fastest ET for the oxidation process afforded by O-CSFS.

Electrochemical performance of these catalysts was further examined by LSV curves as shown in Fig. 5(c). At 10 mA/cm^2, an initial potential of 1.740 V vs. RHE was afforded by Fe-Co$_3$O$_4$/GCE, while CCFCF@C, CCFCF@C-50, CCFCF@C-70, and O-CSFS on GCE needed only 1.651, 1.679, 1.646, and 1.605 V vs. RHE, respectively. By comparison, O-CSFS exhibited the lowest initial potential and the fastest increase in the current density. Similarly, the same order in terms of the initial potential value that was needed to reach 20 mA/cm^2 was also observed. The corresponding overpotentials were displayed in Fig. S8. It

is apparent that O-CSFS demonstrated its outstanding electrochemical performance as it could reach a much lower overpotential of 375 and 402 mV vs. RHE at 10 and 20 mA/cm^2, respectively. The outstanding performance of O-CSFS can be affirmed by the Tafel slope. Fig. 5(d) shows, O-CSFS displayed a Tafel slope of 64.4 mV/dec, which was the lowest among the others (70.2, 100.1, 101.4, and 136.4 mV/dec for CFFCF@C-70, CCFCF@C, CCFCF@C-50, and Fe-Co$_3$O$_4$, respectively), proving its most efficient kinetics behavior.

To better know the conductivity, the interfacial property of the coated electrodes was revealed via EIS and charge transfer resistance (Rct), which was estimated from fitting data using the equivalent circuit model in the inset of Fig. 5(e). The semicircle, which reflected kinetics for ET of each redox species, of O-CSFS/GCE had the smallest diameter, suggesting the lowest resistance (18.20 Ω), possibly due to the magnificent ET behavior and the enhanced interfacial property of O-CSFS. Meanwhile, the largest diameter of the semicircle was observed for Fe-Co$_3$O$_4$/GCE, demonstrating the highest resistance (279.9 Ω). Among CCFCF@C-x/GCE, the CCFCF@C-70/GCE proved intensified charge

Table 2

Summary of all reactions associated with ROS in MPS activation over CCFCF@C and O-CSFS.

ReactionEquation	ReactionEquation
$HSO_5^- \rightarrow H^+ + SO_5^{2-}$ (7)	$SO_4^{\cdot-} + S_2O_8^{2-} \rightarrow SO_4^{2-} + S_2O_8^{\cdot-}$ (27) $k_2 = 1.2 \times 10^6 Lmol^{-1}s^{-1}$
$HSO_5^- + SO_5^{2-} \rightarrow 2SO_4^{2-} + H^+ + {}^1O_2$ (8)	$SO_4^{\cdot-} + H_2O_2 \rightarrow SO_4^{2-} + HO_2^{\cdot} + H^+$ (28) $k_2 = 1.2 \times 10^7 Lmol^{-1}s^{-1} atpH7$
$HSO_5^- + H_2O \rightarrow H_2O_2 + HSO_4^-$ (9)	$HO_2^{\cdot} + HO_2^{\cdot} \rightarrow H_2O_2 + O_2$ (29) $k_2 \sim 8 \times 10^5 Lmol^{-1}s^{-1}$
$H_2O_2 \rightarrow 2\,{}^{\cdot}OH$ (10)	$HO_2^{\cdot} \rightarrow H^+ + O_2^{\cdot-}$ (30)
$HSO_5^- + {}^{\cdot}OH \rightarrow SO_5^{\cdot-} + H_2O$ (11) $k_2 = 2.9 \times 10^8 Lmol^{-1}s^{-1}$	$HO_2^{\cdot} + O_2^{\cdot-} + H^+ \rightarrow H_2O_2 + O_2$ (31) $k_2 \sim 8 \times 10^7 Lmol^{-1}s^{-1}$
$HSO_4^- + {}^{\cdot}OH \rightarrow H_2O + SO_4^{\cdot-}$ (12)	$HO_2^{\cdot} + O_2^{\cdot-} \rightarrow HO_2^- + {}^1O_2$ (32)
$HSO_5^- + SO_4^{\cdot-} \rightarrow SO_4^{2-} + SO_5^{\cdot-} + H^+$ (13)	$HO_2^- + {}^{\cdot}OH \rightarrow OH^- + HO_2^{\cdot} \rightleftharpoons O_2^{\cdot-} + H^+$ (33) $k_2 = 7.5 \times 10^9 Lmol^{-1}s^{-1}$
$4\,{}^{\cdot}OH \rightarrow {}^1O_2 + 2H_2O$ (14)	$HO_2^{\cdot} + {}^{\cdot}OH \rightarrow H_2O + O_2$ (34) $k_2 = 6 \times 10^9 Lmol^{-1}s^{-1}$
$Co(II) + HSO_5^- \rightarrow Co(III) + SO_4^{2-} + {}^{\cdot}OH$ (15)	${}^{\cdot}OH + {}^{\cdot}OH \rightarrow H_2O_2$ (35) $k_2 = 5.5 \times 10^9 Lmol^{-1}s^{-1}$
$Fe(II) + HSO_5^- \rightarrow Fe(III) + SO_4^{2-} + {}^{\cdot}OH$ (16)	${}^{\cdot}OH + H_2O_2 \rightarrow HO_2^{\cdot} + H_2O \rightleftharpoons O_2^{\cdot-} + H^+$ (36) $k_2 = 2.7 \times 10^7 Lmol^{-1}s^{-1}$
$Co(II) + HSO_5^- \rightarrow Co(III) + SO_4^{\cdot-} + OH^-$ (17)	$2O_2^- + 2H_2O \rightarrow {}^1O_2 + H_2O_2 + 2OH^-$ (37)
$Fe(II) + HSO_5^- \rightarrow Fe(III) + SO_4^{\cdot-} + OH^-$ (18)	$2O_2^- + 2H^+ \rightarrow H_2O_2 + {}^1O_2$ (38) $k_2 < 0.2 Lmol^{-1}s^{-1}$
$Co(III) + HSO_5^- \rightarrow Co(II) + SO_5^{\cdot-} + H^+$ (19)	$O_2^- + {}^{\cdot}OH \rightarrow {}^1O_2 + OH^-$ (39) $k_2 = 8 \times 10^9 Lmol^{-1}s^{-1}$
$Co(III) + Fe(II) \rightarrow Co(II) + Fe(III)$ (20)	$O_2^{\cdot-} + H_2O_2 \rightarrow {}^{\cdot}OH + OH^- + O_2$ (40) $(Haber-Weissreaction)$
$SO_5^{\cdot-} \rightarrow SO_4^{\cdot-} + 1/2O_2$ (21)	$Fe(II) + H_2O_2 \rightarrow Fe(III) + {}^{\cdot}OH + OH^-$ (41) $k_2 = 40 \sim 80 Lmol^{-1}s^{-1}$
$4SO_5^{\cdot-} + 2H_2O \rightarrow 4HSO_4^- + 3\,{}^1O_2$ (22)	$Co(III) + H_2O_2 \rightarrow Co(II) + HO_2^{\cdot} + H^+$ (42)
$2SO_5^{\cdot-} \rightarrow S_2O_8^{2-} + {}^1O_2$ (23)	$Fe(III) + H_2O_2 \rightarrow Fe(II) + HO_2^{\cdot} + H^+$ (43) $k_2 = 9.1 \times 10^{-7} Lmol^{-1}s^{-1}$
$SO_4^{\cdot-} + H_2O \rightarrow SO_4^{2-} + {}^{\cdot}OH + H^+$ (24) $k_2 < 3 \times 10^3 Lmol^{-1}s^{-1}$	$Fe(III) + HO_2^{\cdot} \rightarrow Fe(II) + O_2 + H^+$ (44) $k_2 = 0.33 \sim 2.1 \times 10^6 Lmol^{-1}s^{-1}$
$SO_4^{\cdot-} + OH^- \rightarrow SO_4^{2-} + {}^{\cdot}OH$ (25) $k_2 = 6.5 \times 10^7 Lmol^{-1}s^{-1} (alk.)$	$S_2^{2-} + 14Co(III) + 8OH^- \rightarrow 2SO_4^{2-} + 14Co(II) + 8H^+$ (45)
$SO_4^{\cdot-} + SO_4^{\cdot-} \rightarrow S_2O_8^{2-}$ (26) $k_2 = 8.1 \times 10^8 Lmol^{-1}s^{-1} pH5.8$	$S_2^{2-} + 14Fe(III) + 8OH^- \rightarrow 2SO_4^{2-} + 14Fe(II) + 8H^+$ (46)

transfer efficiency (27.35 Ω), resulted from high surface area as well as lattice and carbon defects of CCFCF@C-70. On the contrary, the lower diameter of CCFCF@C than CCFCF@C-50 but larger than that of CCFCF@C-70 was largely as a result of its highest surface area (Fig. 2(n)) and carbon defects (Fig. 4(d)). The Rct value of these two electrodes was 35.58 and 89.96 Ω for CCFCF@C and CCFCF@C-50, respectively. Further, O-CSFS also had the highest C_{dl} value of 7.27 mF/cm^2 (Fig. 5 (f)), which was obtained from the slope of linear relationship between ΔJ and scan rate in Fig. S9, Thus, it had the highest ECSA of 12.847 cm^2, suggesting O-CSFS had plenty of accessible-active sites.

3.8. Comparing catalytic PCM degradation under different conditions

The performance towards MPS activation was evaluated via PCM degradation. Fig. 6(a) shows MPS itself degraded marginally PCM, suggesting limited generation of ROS from self-decomposition. On the other hand, a little PCM was found to be adsorbed by CCFCF@C and even almost no by O-CSFS, proving the minor role of physical adsorption. All the catalysts combined with MPS enabled PCM to degrade much effectively, suggesting their positive role in activating MPS. Among CCFCF@C-x, CCFCF@C-70 had the highest performance, followed by CCFCF@C and CCFCF@C-50. Higher performance of CCFCF@C-70 than CCFCF@C was possibly because of its higher contents of Co(II) and Fe(II) (Fig. 4(k)). However, CCFCF@C could show the efficiency in degradation of PCM comparable to that of CCFCFC@C-70, which could be resulted from higher surface area (28.6315 m^2/g) and enrichment in lattice and carbon defects. Although CCFCF@C-50 had the highest OV content, its performance was the most inferior, suggesting the lower role of OV than lattice and carbon defects as well as Co(II) content. Different from the others, O-CSFS exhibited the most superior performance, suggesting the preeminence of the sulfidation and the successful enhancement of Fe-Co$_3$O$_4$ performance via sulfidation (Fig. 6(a)). Furthermore, the degradation of PCM over these catalysts was observed to comply with the first order reaction (Eq. (6)) as shown in Fig. 6(b).

$$\ln(C_t/C_0) = -kt \qquad (6)$$

Accordingly, k value of these catalysts was in the order of Fe-Co$_3$O$_4$ (0.8413 min^{-1}) < CCFCF@C-50 (1.1083 min^{-1}) < CCFCF@C (1.4654 min^{-1}) < CCFCF@C-70 (3.6218 min^{-1}) < O-CSFS (4.9239 min^{-1}), demonstrating the most powerful performance of O-CSFS.

The degradation of PCM is believed to come from the efficiency of activating MPS. As Fig. 6(c) and Fig. S10 show, the PCM degradation was found to be positively correlated to MPS decomposition performance of O-CSFS, proving the effective sulfidation, which later induced lattice defect as well as SV and oxygen doping, thereby accounting for the highest performance of O-CSFS [17].

Effects of different factors on the performance of O-CSFS was further evaluated. Fig. S11(a) shows the PCM degradation was almost independent of O-CSFS amount, indicating outstanding performance of O-CSFS. MPS amount in Fig. S11(b), on the other hand, showed its significant effect. The PCM degradation was accelerated as increasing MPS amount, and total degradation was obtained within 1.5 min at 200 mg/L MPS, which could be explained by the amount of ROS generated from it [37]. Also, the performance of O-CSFS was positively related to MPS loading and a high PCM degradation efficiency was achieved at high MPS concentration. Quite similar to MPS, the behavior of PCM degradation was also affected by its concentration but to a lesser extent (Fig. S11(c)), possibly because of the increased obstruction of active sites by increased amount of PCM [37]. Effects of inorganic anions and HA were also taken into account. Fig. S11(d) shows CO_3^{2-} and HA had the most obvious effects on PCM degradation, while the efficiency still remained unchanged with and without the presence of Cl^-, NO_3^-, and HCO_3^-, suggesting good resistance to high concentration of anions of O-CSFS. However, the inhibitory effect of CO_3^{2-} could be attributed to the transformation of $^{\bullet}OH/SO_4^{\bullet-}$ to $CO_3^{\bullet-}$ with a lower potential, and the effect of HA was mainly because of its adhesion to the surface of O-CSFS [37]. As pH is considered to have great influences on catalytic degradation of pollutants. Thus, its effect on PCM degradation in O-CSFS/MPS system was investigated. In Fig. S12(a), effects of different pH values were exhibited. Although PCM degradation efficiency dropped slightly to 86.72% at pH 11, almost no significant differences were found at pH from 3 to 9, implying the high adaptability of O-CSFS to a wide pH range. The deterioration in efficiency at pH 11 could be deemed as a result of increase in MPS consumption (Fig. S13). In addition, electrostatic repulsion between negatively charged O-CSFS and anionic PCM species (pk$_a$ of PCM = 9.46 [48]) could also be another cause (Fig. S12 (b)). In the case where $^{\bullet}OH$ and $SO_4^{\bullet-}$ are involved in the degradation, the weakening of the oxidation potential of $^{\bullet}OH$ and the conversion of $SO_4^{\bullet-}$ to $^{\bullet}OH$ at high pH (k = 8.3 ×10^7 L mol^{-1} s^{-1}) [49] could not be ignored. For comparison, effects of pH on CCFCF@C for PCM degradation were also investigated. Zeta potential in Fig. S12(b) and results in Fig. S15 could explain the effects of pH in Fig. S14. To evaluate the potential of O-CSFS, DI water was replaced with tap and sea waters. As a

Table 3
Summary of direct reactions with electrons[a] in CCFCF@C/MPS[b] and O-CSFS/MPS[c] systems.

ReactionEquation	ReactionEquation
$O_2 + e_{aq}^- \rightarrow O_2^{\cdot-}(47) k_2 = 1.9 \times 10^{10} Lmol^{-1}s^{-1}(-0.33 V vs. NHE)$	$Fe(III) + 2O_{latt}^{2-} \rightarrow Fe(II) + {}^1O_2 + 3e_{aq}^- (62)$
$O_2 + 2H^+ + 2e_{aq}^- \rightarrow H_2O_2 (+0.68 V vs. NHE)(48)$	$Co(III) + e_{aq}^- \rightarrow Co(II)(63)$
$O_2^{\cdot-} + e_{aq}^- + 2H^+ \rightarrow H_2O_2(+1.44 V vs. NHE)(49)$	$Fe(III) + e_{aq}^- \rightarrow Fe(II)(64)$
$O_2^{\cdot-} + e_{aq}^- \rightarrow O_2^{2-} k_2 = 1.3 \times 10^{10} Lmol^{-1}s^{-1}(50)$	$S^{2-} + SO_4^{2-} + 8H^+ + 10e_{aq}^- \rightarrow 3S^{2-} + 4H_2O(65)$
$H_2O_2 + e_{aq}^- + H^+ \rightarrow {}^\cdot OH + H_2O(51)$	$2S^{2-} + 2Co(III) \rightarrow S_2^{2-} + 2Co(II)(66)$
$H_2O_2 + e_{aq}^- \rightarrow OH^- + {}^\cdot OH(52) k_2 = 1.1 \times 10^{10} Lmol^{-1}s^{-1}$	$2S^{2-} + 2Fe(III) \rightarrow S_2^{2-} + 2Fe(II)(67)$
$HO_2^- + e_{aq}^- \rightarrow 2OH^- + {}^\cdot OH(53) k_2 = 3.5 \times 10^9 Lmol^{-1}s^{-1}$	$S_2^{2-} + 4HSO_5^- + 2e_{aq}^- \rightarrow 2SO_4^{2-} + 4SO_3^{2-} + 4H^+(68)$
$HSO_5^- + e_{aq}^- \rightarrow SO_4^{\cdot-} + OH^-(54)$	$SO_3^{2-} + Co(III) \rightarrow SO_3^{\cdot-} + Co(II)(69)$
$HSO_5^- + e_{aq}^- \rightarrow SO_4^{2-} + {}^\cdot OH(55)$	$SO_3^{2-} + Fe(III) \rightarrow SO_3^{\cdot-} + Fe(II)(70)$
${}^\cdot OH + e_{aq}^- + H^+ \rightarrow H_2O(56)$	$SO_3^{2-} + {}^\cdot OH \rightarrow SO_3^{\cdot-} + OH^-(71) E \ of \ SO_3^{\cdot-} = +0.84 \ V \ vs. \ NHE \ at \ pH \ 3.6, = +0.63 \ V \ vs. \ NHE \ at \ pH \ 7$
${}^\cdot OH + e_{aq}^- \rightarrow OH^-(57) k_2 = 3 \times 10^{10} Lmol^{-1}s^{-1} at pH10.5$	$SO_3^{\cdot-} + SO_3^{\cdot-} \rightarrow S_2O_6^{2-}(72) k_2 = 2.7 \times 10^8 \sim 9.5 \times 10^8 Lmol^{-1}s^{-1}$
$S_2O_8^{2-} + e_{aq}^- \rightarrow SO_4^{\cdot-} + SO_4^{2-}(58) k_2 = 1.1 \times 10^{10} Lmol^{-1}s^{-1}$	$SO_3^{\cdot-} + O_2 \rightarrow SO_5^{\cdot-}(73) k_2 = 1.5 \times 10^9 Lmol^{-1}s^{-1} at pH6.8$
$SO_4^{\cdot-} + e_{aq}^- + H^+ \rightarrow HSO_4^-(59)$	$SO_5^{\cdot-} + SO_3^{2-} \rightarrow SO_4^{\cdot-} + SO_4^{2-}(74)$
$O_2 + 4e_{aq}^- \rightarrow 2O_{latt}^{2-}(60)$	$SO_5^{\cdot-} + SO_3^{2-} + H^+ \rightarrow SO_3^{\cdot-} + HSO_5^-(75) k_2 = 1.3 \times 10^7 Lmol^{-1}s^{-1} at pH8.7$
$Co(III) + 2O_{latt}^{2-} \rightarrow Co(II) + {}^1O_2 + 3e_{aq}^-(61)$	$S_2O_8^{2-} + e_{aq}^- \rightarrow SO_4^{\cdot-} + SO_4^{2-}(76) k_2 = 1.2 \times 10^{10} Lmol^{-1}s^{-1}$

(a) Except for Eqs. (61, 62) and Eqs. (66, 67, 69–75), which might occur after Eq. (60) and Eqs. (65, 68), respectively; (b) For Eqs. (47–64, 76); and (c) For Eqs. (47–76).

result, 92.33% and 88.33% PCM were degraded in tap and sea waters, respectively, which were comparable to the degradation efficiency in DI water (Fig. S16(a)), further validating the feasibility of O-CSFS in practical applications. In fact, the existence of inorganic anions in tap water and high Cl$^-$ concentration in seawater could react with ROS to form other species with lower potential, and thereby lowering the degradation efficiency. Moreover, the stability of O-CSFS was also examined via five-cycle repeated degradation (Fig. S16(b)). The degradation efficiency of PCM still remained quite stable util the third cycle, and only a slight decline was observed in the next two cycles, proving that O-CSFS could be used to degrade PCM effectively for long time. This could be because of slight decrease in surface area (Fig. S16(c, d)) as well as no changes in XRD pattern (Fig. S17) between before and after reaction.

3.9. Tracing ROS

A variety of ROS could be generated from MPS activation over metal-based catalysts [3,50]. The contribution of these species to PCM degradation over CCFCF@C and O-CSFS can be detected by using various scavengers.

As TBA would rather react with $^\cdot OH$ than with $SO_4^{\cdot-}$ (k_2 vs $^\cdot OH$ = 3.8–7.6 $\times 10^8$ L mol^{-1} s^{-1} > k_2 vs $SO_4^{\cdot-}$ = 4–9.5 $\times 10^5$ L mol^{-1} s^{-1}) and MeOH prefers reacting selectively with both $^\cdot OH$ and $SO_4^{\cdot-}$ (k_2 vs $^\cdot OH$ = 9.7 $\times 10^8$ L mol^{-1} s^{-1}, k_2 vs $SO_4^{\cdot-}$ = 2.5 $\times 10^7$ L mol^{-1} s^{-1}) [49]. Fig. 6(d, e) depict that regardless of how much TBA was used, the degradation of PCM still proceeded without any decline, suggesting either no $^\cdot OH$ generation or no contribution of $^\cdot OH$ to PCM degradation over CCFCF@C and O-CSFS. MeOH, on the other hand, exerted its obvious effect on reducing PCM degradation from 83.79% to 56.47% for CCFCF@C and from 38.15% to 13.99% for O-CSFS as increasing MeOH concentration from 0.2 M to 0.5 M, revealing the existence of $SO_4^{\cdot-}$ as well as its contribution to the PCM degradation. Similar effects could be seen for NaN$_3$, a scavenger for $^1O_2$ with k_2 = 1.0 $\times 10^9$ L mol^{-1} s^{-1} [17,51], in both CCFCF@C/MPS and O-CSFS/MPS systems, partly proving a certain role of $^1O_2$ in degrading PCM.

It is reported that the origin of $^1O_2$ could come from $O_2^{\cdot-}$ as an intermediate via direct oxidation by water (Eq. (37)) [52], by H$^+$ (Eq. (38)) [17], or by $^\cdot OH$ (Eq. (39)) [17] (Table 2). For other equations if mentioned, please refer to Tables 2, 3. Also, no contribution of $^\cdot OH$ to PCM degradation was found. Thus, the indication as to whether $O_2^{\cdot-}$ is

present could be identified by p-BQ (k_2 vs $O_2^{\cdot-}$ = 2.9 $\times 10^9$ L mol^{-1} s^{-1} [17,53]) although p-BQ could react with $^\cdot OH$ at a high rate constant of 1.2 $\times 10^9$ L mol^{-1} s^{-1} [53]. It is apparent from Fig. 6(d, e) that PCM degradation was inhibited to a larger extent with increasing p-BQ concentration from 0.2 to 0.5 mM in both CCFCF@C/MPS and O-CSFS/MPS systems. These results, therefore, show that $O_2^{\cdot-}$ was likely to be generated, participated in PCM degradation, and might act as an intermediate for $^1O_2$ generation.

To evidence the above ROS, electron paramagnetic resonance (EPR) analysis was employed (Text S5). As shown in Fig. 6(f), several peaks typical of DEMPO-$^\cdot OH/SO_4^{\cdot-}$ were observed. Compared with sole MPS, CCFCF@C/MPS or O-CSFS/MPS generated these peaks with higher intensity, once again endorsing the actual role of CCFCF@C and O-CSFS in activation of MPS. When PCM was coexisted in the detection solution, the intensity of these peaks was augmented in case of CCFCF@C/MPS, but was weakened in case of O-CSFS/MPS. This implies that the generated $^\cdot OH/SO_4^{\cdot-}$ was either consumed by PCM in O-CSFS/MPS system or limited by less exposed active sites of O-CSFS due to the blocking effect of PCM. If the consumption by PCM is the case, $^\cdot OH/SO_4^{\cdot-}$ directly contribute to PCM degradation. In this regard, the actual contribution of $^\cdot OH$ would be excluded as no conspicuous effect of TBA was found in the scavenging tests above. On the other hand, the enhancement of these peaks caused by PCM in CCFCF@C/MPS system means that PCM might act as an electron donor, pushing up the generation of $^\cdot OH/SO_4^{\cdot-}$ [37]. For this reason, the degradation route of PCM in CCFCF@C/MPS system would not be dominated by PCM-enhanced $^\cdot OH/SO_4^{\cdot-}$ generation although $^\cdot OH/SO_4^{\cdot-}$ generation was higher in the presence of PCM.

To unravel the role of $^\cdot OH/SO_4^{\cdot-}$, further experiments on MPS decomposition over CCFCF@C and O-CSFS were performed. As 0.2 M TBA speeded up the MPS consumption for both CCFCF@C and O-CSFS, and 0.5 M TBA restricted, but accelerated the MPS consumption for CCFCF@C and O-CSFS, respectively (Fig. S18(a, b)), the PCM degradation would be affected. However, the results in Fig. 6(d, e) were rather contrary, suggesting possibly other ROS rather than $^\cdot OH$ might be involved in the degradation. Similar inhibitory effect was also seen for MeOH in case of CCFCF@C but not O-CSFS (Fig. S18(c, d)), indicating $SO_4^{\cdot-}$ indeed took part in PCM degradation over O-CSFS, while the role of $SO_4^{\cdot-}$ in CCFCF@C/MPS system for PCM degradation was limited. At the same time, this means that the MeOH-induced decline in PCM degradation in CCFCF@C/MPS system was partly because of the
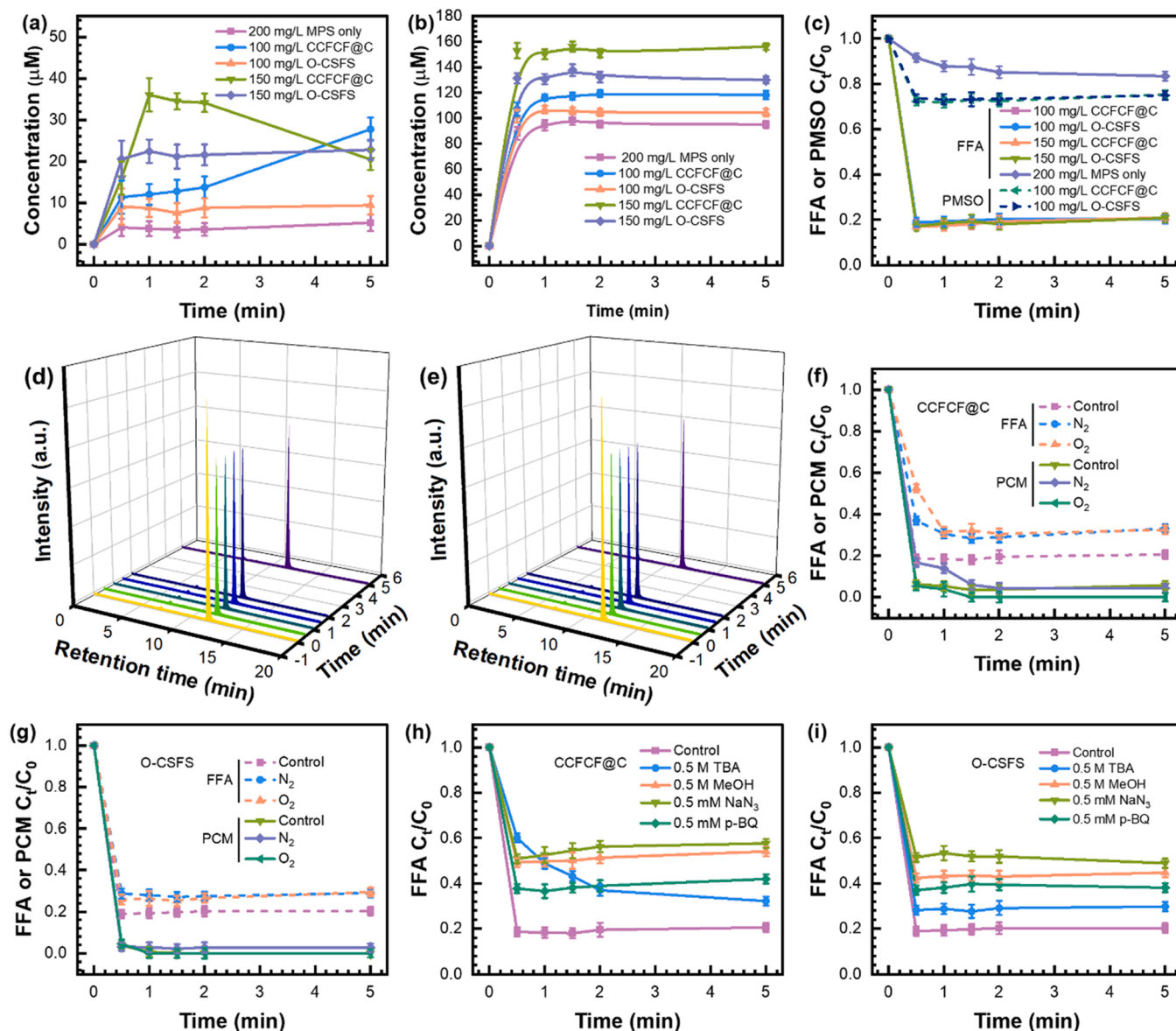
Fig. 7. Generation of (a) $^{\bullet}OH$ and (b) $SO_4^{\bullet-}$, (c) FFA/PMSO loss over MPS with and without CCFCF@C and O-CSFS at different amounts (catalysts = 100/150 mg/L for $^{\bullet}OH/SO_4^{\bullet-}$ and FFA; catalysts = 100 mg/L for PMSO; MPS = 200 mg/L; BA = 0.4 mM; 4-HBA = 0.3 mM; FFA = 0.75 mM; PMSO = 2 mM; and t = 30 °C); (d, e) chromatograms of PMSO loss over (d) CCFCF@C and (e) O-CSFS; (f, g) FFA loss and PCM degradation over (f) CCFCF@C and (g) O-CSFS with and without N_2/O_2 bubbling; (h, i) FFA loss over (h) CCFCF@C and (i) O-CSFS with and without different scavengers (catalysts = 100 mg/L, MPS = 200 mg/L, PCM = 20 mg/L, FFA = 0.75 mM, and T = 30 °C).

aggregation of CCFCF@C caused by carbon chain of MeOH [54]. These results are found to quite reasonable because of lower reaction rate of $^{\bullet}OH$ with PCM (1.2×10^9 L mol^{-1} s^{-1}, protonated) than $SO_4^{\bullet-}$ with PCM (4.7×10^9 L mol^{-1} s^{-1}, protonated) [55].

In addition, EPR signals generated by the addition reaction of TEMP with $^1O_2$ were also analyzed. Fig. 6(g) confirms the presence of these peaks, which produced by CCFCF@C/MPS were slightly intensified in comparison with those produced by sole MPS, and remained almost unchanged as PCM was added. In contrast, it would seem that not enough $^1O_2$ was generated to raise the intensity in either O-CSFS/MPS or O-CSFS/MPS/PCM system. Thus, it could be argued that $^1O_2$ might play a certain role in PCM degradation in case of CCFCF@C as the quenching test with NaN$_3$ showed an obvious decline in the performance of CCFCF@C, while it would be trivial in case of O-CSFS. However, NaN$_3$ rather diminished the PCM degradation over O-CSFS, suggesting the possible side effect of NaN$_3$. To support this, the decomposition of MPS in the presence of NaN$_3$ would be used. Not contrary to the expectation,

Fig. S18(f) shows a fairly close agreement that the enhanced MPS consumption as raising the NaN$_3$ concentration was clearly the main reason [56]. Similarly, the same effect was also observed in CCFCF@C/MPS system (Fig. S18(e)), meaning that $^1O_2$ was actually generated by MPS activation over CCFCF@C and O-CSFS, but was negligible. On this account, it is quite unclear that whether or not there was any contribution of $^1O_2$ to PCM degradation over CCFCF@C. Additional experiments on FFA loss are, therefore, needed. This will be mentioned in the later section.

As showed by the decline in PCM degradation due to the addition of p-BQ, the generation of $O_2^{\bullet-}$ was probable. EPR spectra in Fig. 6(h) show the signals typical of 5,5-dimethyl-2-pyrrolidone-N-oxyl (DMPOX) instead of DMPO-$O_2^{\bullet-}$ appeared, demonstrating the absence of $O_2^{\bullet-}$ in both CCFCF@C/MPS and O-CSFS/MPS systems. According to a recent study, the generation of other new species from $O_2^{\bullet-}$ could account for this [17]. Furthermore, it is also possible that the generated $O_2^{\bullet-}$ might mainly exist in the form of surface-bound radical (i.e., no $O_2^{\bullet-}$ in the

solution was present), and thus the failure in detection of DMPO-$O_2^{\bullet-}$ signals could be easily understood. Nonetheless, the inhibitory effect induced by p-BQ contradicted this. Therefore, it is necessary to detect $O_2^{\bullet-}$ using an appropriate chemical probe. As NBT can be reduced by $O_2^{\bullet-}$ at a rate constant of $5.76\text{–}6.04 \times 10^4$ L mol^{-1} s^{-1} to form mono-formazan at 530 nm [57], the generation of $O_2^{\bullet-}$ could be then detected by using NBT as a probing agent. Unfortunately, the generation of monoformazan could not observed, meaning that $O_2^{\bullet-}$ was generated in neither CCFCF@C/MPS nor O-CSFS/MPS systems. Also, it is quite curious that despite the absence of $O_2^{\bullet-}$, p-BQ attenuated the degradation of PCM. The decomposition of MPS in the presence of p-BQ could explain this clearly. As can be seen from the results in Fig. S18(g, h), the enhanced consumption of MPS with increasing p-BQ concentration was rather the underlying cause.

3.10. Probing $^{\bullet}OH/SO_4^{\bullet-}$ and $^1O_2$ generation

The generation of 4-HBA and p-BQ as a result of combining $^{\bullet}OH$ and $SO_4^{\bullet-}$ with BA (k_2 of $^{\bullet}OH$ vs BA = 4.2×10^9 L mol^{-1} s^{-1} [37,58] > k_2 of $SO_4^{\bullet-}$ vs BA = 1.2×10^9 L mol^{-1} s^{-1} [59]) and 4-HBA (k_2 of $SO_4^{\bullet-}$ vs 4-HBA = 2.5×10^9 L mol^{-1} s^{-1} [59] > k_2 of $^{\bullet}OH$ vs 4-HBA = 2.19×10^9 L mol^{-1} s^{-1} [60]), respectively were quantified to determine $^{\bullet}OH$ and $SO_4^{\bullet-}$ amounts produced by CCFCF@C and O-CSFS-activated MPS.

From Fig. 7(a, b), sole MPS at 200 mg/L decomposed by itself to generate limited amount of $^{\bullet}OH/SO_4^{\bullet-}$, which was lower than those produced by coupling either 100 mg/L CCFCF@C or 100 mg/L O-CSFS with MPS at the same concentration (i.e., 200 mg/L). The amount of generated $^{\bullet}OH/SO_4^{\bullet-}$ was even enhanced to a higher extent when 150 mg/L CCFCF@C or O-CSFS was adopted. Thus, it is quite reasonable to say that these results were in good agreement with those observed on the EPR spectra (Fig. 6(f)), further confirming that $^{\bullet}OH/SO_4^{\bullet-}$ were actually generated but the contribution of $^{\bullet}OH$ to PCM degradation would be ruled out. Meanwhile, the generated $SO_4^{\bullet-}$ might be responsible partly for PCM degradation in CCFCF@C/MPS but significantly in O-CSFS/MPS system.

In addition, it is also questioned whether $^1O_2$ was the predominant species accounting for PCM degradation induced by CCFCF@C-activated MPS or not as the generation of $SO_4^{\bullet-}$ in CCFCF@C/MPS system was obviously higher than that in O-CSFS/MPS system, while the performance of O-CSFS for PCM degradation was higher. The role of $^1O_2$ in this case is, therefore, needed to clarify this concern by using the FFA loss profile. Fig. 7(c) manifests a far higher FFA loss caused by CCFCF@C/MPS and O-CSFS/MPS than that caused by sole MPS. Nevertheless, the increase in CCFCF@C or O-CSFS amount to a magnitude of 1.5 did not elevate the loss of FFA anymore, intimating the limited amount of $^1O_2$ generated by CCFCF@C or O-CSFS-activated MPS. Further, it is notable that the TEMP-$^1O_2$ signals of O-CSFS/MPS were less intense than those of CCFCF@C/MPS, while the FFA loss induced by both CCFCF@C/MPS and O-CSFS/MPS was likely the same. This could stem from possible difference in $^1O_2$ capture by TEMP between the bulk solution and the O-CSFS surface [37]. Overall, it is quite strange that O-CSFS had a higher performance than CCFCF@C in spite of its lower $SO_4^{\bullet-}$ generation as well as its almost similar FFA loss, enunciating that neither $SO_4^{\bullet-}$ nor $^1O_2$ accounted for greater performance of O-CSFS.

Recently, high-valent transition metal oxo-species have been reported to appear from MPS activation systems associated with metal-based catalysts [61,62]. Therefore, it would be reasonable to argue that such high-valent species might be existed in O-CSFS/MPS system. PMSO has been adopted as probing agent for high-valent transition metal oxo-species so far as it could be easily oxidized by these high-valent species at a high-rate constant of 2.0×10^6 L mol^{-1} s^{-1} (for Co(IV) [61]) or 1.23×10^5 L mol^{-1} s^{-1} (for Fe(IV) at pH 1 [63]) to form PMSO$_2$. However, Fig. 7(c) exhibits the loss of PMSO was rather caused by other ROS (k_2 vs $^{\bullet}OH = 3.61 \times 10^9$ L mol^{-1} s^{-1}, k_2 vs $SO_4^{\bullet-} = 3.17 \times 10^8$ L mol^{-1} s^{-1} [63]). In addition, there was no any indication

showing the appearance of PMSO$_2$ on the chromatogram in Fig. 7(d, e). For this reason, such high-valent species would be disregarded. In other words, it remains unclear that whether or not other active species might be overlooked. This concern, therefore, should be taken into account.

Despite the minor role in PCM degradation (low k_2 of $^1O_2$ vs PCM = 3.35×10^6 L mol^{-1} s^{-1}, protonated [55]) as demonstrated by limited amount of generated $^1O_2$ (Fig. 7(c)) and the decline in PCM degradation resulted from increased consumption of MPS rather than actual scavenging effect of NaN$_3$ (Fig. S18(e, f)), the presence of $^1O_2$ in CCFCF@C/MPS and O-CSFS/MPS systems finds it quite curious to dig deep into the origin of $^1O_2$. On the one hand $^1O_2$ could be generated from $O_2^{\bullet-}$ as an intermediate, but on the other hand, it is usually accepted that oxygen can be reduced by electrons from electron-rich sites on the surface of catalysts into $O_2^{\bullet-}$ via Eq. (47).

By this way, the generation of $^1O_2$ depends on $O_2^{\bullet-}$, and hence the depletion of $O_2^{\bullet-}$. This is quite reasonable because the DMPO-$O_2^{\bullet-}$ could not be detected as well as monoformazan was not formed. If $O_2^{\bullet-}$-dependent $^1O_2$ generation is the case, the PCM degradation will be diminished to a certain extent upon bubbling N$_2$ as $O_2^{\bullet-}$ could not be produced without O$_2$ as well as the minor role of $^1O_2$ as examined above. Fig. 7(f, g) display PCM degradation and FFA loss in CCFCF@C/MPS and O-CSFS/MPS systems. Considering PCM, greater decline in the efficiency, therefore, could be seen in CCFCF@C/MPS system than in O-CSFS/MPS system, revealing the possibly greater $O_2^{\bullet-}$-dependent generation of $^1O_2$ induced by CCFCF@C-activated MPS. Once O$_2$ was bubbled, the PCM degradation in CCFCF@C/MPS system was enhanced slightly, while no obvious difference could be seen any more in O-CSFS/MPS system. The results further disclose that the generation of $^1O_2$ in CCFCF@C/MPS system might be accompanied by $O_2^{\bullet-}$ that stemmed from externally-supplied O$_2$. Meanwhile, the association between $^1O_2$ generation and $O_2^{\bullet-}$ in O-CSFS/MPS system would seem possible but not obvious, or rather the insignificant amount of $^1O_2$ resulted from $O_2^{\bullet-}$. To sum up, extra experiments on FFA loss would be useful to confirm this speculation. The reduced FFA loss under either N$_2$ or O$_2$ bubbling in CCFCF@C/MPS and O-CSFS/MPS systems compared to the control ones (Fig. 7(f, g)) suggest $O_2^{\bullet-}$ might be directly responsible for $^1O_2$ generation, and either the adsorbed O$_2$ on the surface of CCFCF@C and O-CSFS or O$_2$ resulted from $SO_5^{\bullet-}$ disproportionation via Eq. (21) [17] rather than externally-supplied O$_2$ was likely to be the precursor for $O_2^{\bullet-}$ formation (as no increase in FFA loss was found when O$_2$ was supplied). However, O$_2$ resulted from $SO_5^{\bullet-}$ disproportionation and externally-supplied O$_2$ would be the same in terms of characteristics.

In this case, the reason why O$_2$ bubbling reduced the FFA loss needs to be clarified. As shown in Fig. 7(f), O$_2$ bubbling rather enhanced slightly PCM degradation in CCFCF@C/MPS system. This manifests that the externally-supplied O$_2$ might account for the generation of other ROS rather than $O_2^{\bullet-}$. The formation of $SO_4^{\bullet-}$ via Eq. (21) after Eqs. (10,11, 48) could be considered. With high reaction rate of $SO_4^{\bullet-}$ with PCM (4.7×10^9 L mol^{-1} s^{-1}, protonated [55]), the formation of $SO_4^{\bullet-}$ by this way could easily account for higher PCM degradation in CCFCF@C/MPS system upon bubbling O$_2$.

As $SO_4^{\bullet-}$ could react with OH$^-$/H$_2$O to form $^{\bullet}OH$ (Eqs. (24, 25) [49, 64]) and $^{\bullet}OH$ later would undergo disproportionation to form $^1O_2$ via Eq. (14). However, $^{\bullet}OH$ could react preferably with FFA at a high reaction rate of 1.5×10^{10} L mol^{-1} s^{-1} before being disproportionated. Then the consumption of FFA by $^{\bullet}OH$ would also increase the FFA loss, but the fact remains that the FFA loss by either CCFCF@C or O-CSFS-activated MPS was rather inhibited by O$_2$ bubbling (Fig. 7(f, g)). Therefore, Eqs. (14, 24, 25) actually did not occur.

In summary, the decline in FFA loss and PCM degradation by N$_2$ bubbling suggests $^1O_2$ was generated from $O_2^{\bullet-}$ as an intermediate. The inhibitory effect of O$_2$ bubbling on FFA loss, on the other hand, was explained by the increased generation of $SO_4^{\bullet-}$ rather than $^1O_2$. Without O$_2$ bubbling, the generation of $^1O_2$ induced the loss of FFA. When O$_2$ was bubbled, the activation pathway of MPS was regulated by the generation of $SO_4^{\bullet-}$ instead of $^1O_2$, hence the decline in FFA loss.
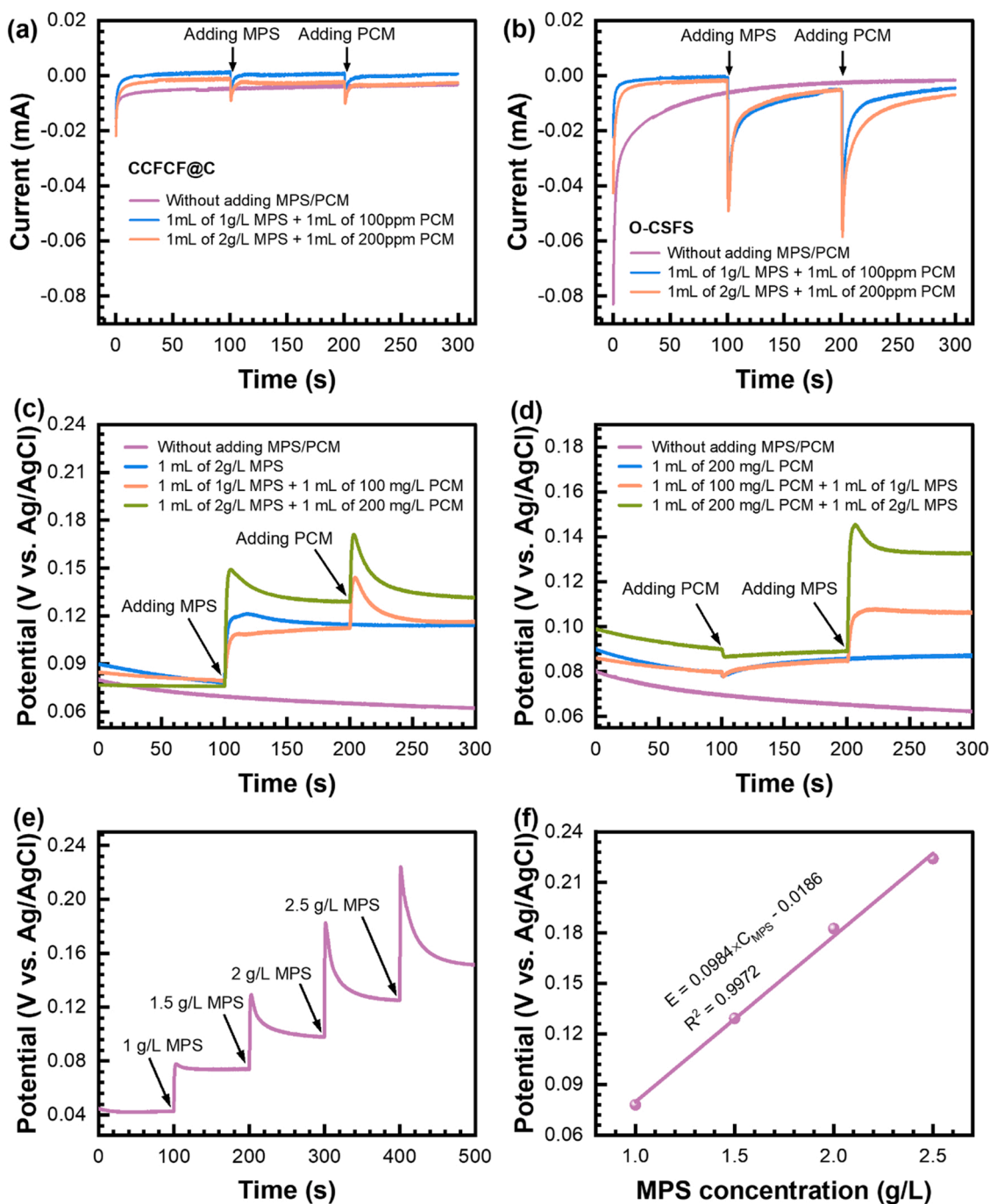
Fig. 8. (a, b) Current responses of (a) CCFCF@C/GCE and (b) O-CSFS/GCE with and without adding MPS/PCM; (c, d) OCP curves of O-CSFS/GCE with and without adding MPS/PCM; (e) changes in potential of O-CSFS/GCE with increasing MPS concentration; and (f) linear relationship between MPS concentration and O-CSFS/GCE potential.

As verified above, the generation of $^1O_2$ from $^•OH$ after Eqs. (24, 25) was not realistic, but whether $^•OH$ from other sources, such as H_2O_2 from Eq. (9) through Eq. (9) and MPS activation by Co(II)/Fe(II) via Eqs. (15, 16), that might cause $^1O_2$ to form via Eq. (14) was still vague. FFA loss under effect of TBA, therefore, would be necessary. Fig. 7(h, i) show the addition of 0.5 M TBA caused a drop in FFA loss by CCFCF@C and O-CSFS-activated MPS to a certain extent, enunciating the feasibility Eq. (14), i.e., $^1O_2$ was also generated from $^•OH$ besides $O_2^{•-}$. Additionally, $O_2^{•-}$ could also react with H_2O_2 via Eq. (40) to form $^•OH$ [65], which subsequently disproportionated to form $^1O_2$ via Eq. (14). Therefore, the TBA-induced decrease in FFA loss would make Eq. (14) more realizable.

Similarly, the same effect on FFA loss cause by 0.5 M MeOH was also seen in both CCFCF@C/MPS and O-CSFS/MPS systems, signifying $SO_4^{•-}$ might act as a precursor for $^1O_2$ generation via Eqs. (14, 24, 25). In this case, the generation of $SO_4^{•-}$ from other sources, for example Eqs. (17, 18), rather than externally-supplied O_2 via Eqs. (10, 11, 48) and then Eq. (21) was taken into account.

For p-BQ, the decline in FFA loss by both CCFCF@C and O-CSFS-activated MPS further confirms the mediate role of $O_2^{•-}$ in the generation of $^1O_2$. Finally, compared to other scavengers, the effect of NaN$_3$ was most obvious, partly suggesting its capturing effect towards $^1O_2$. In addition, its high reaction rate with $SO_4^{•-}$ (2.52×10^9 L mol^{-1} s^{-1} at 24.4 ^{0}C [66]) also deserves consideration as $SO_4^{•-}$ could also play a certain role in $^1O_2$ generation as demonstrated above. Overall, the generation of

$^1O_2$ in CCFCF@C/MPS and O-CSFS/MPS systems was associated with $^\bullet OH$, $SO_4^{\bullet -}$, $O_2^{\bullet -}$.

3.11. Examining intrinsic electron transfer of O-CSFS

To date, mechanisms for MPS activation have been well established with the involvement of radials or non-radicals, in which radicals are usually driven by $^\bullet OH/SO_4^{\bullet -}/O_2^{\bullet -}$. Meanwhile, non-radicals are contributed by $^1O_2$, high-valent transition metal oxo-species, and ET. While high-valent transition metal oxo-species was absent, the role of each ROS was well distinguished. However, these ROS could not comfortably explain the higher performance of O-CSFS. On this account, ET seems like an underlying route accelerating the PCM degradation in O-CSFS/MPS system.

ET firstly could be examined by the promoted consumption of MPS in the presence of PCM [54]. It is observed from Fig. S19(a, c, e) that MPS decomposition over CCFCF@C was barely accelerated as 20 mg/L PCM was added. Meanwhile, the same amount of PCM was employed in O-CSFS/MPS system, a sharp decrease in MPS was undergone (Fig. S19 (b, d, f)). This could be due to the fact that PCM acted as an electron donor, providing more electrons for MPS to be reduced via O-CSFS as an electron mediator [37]. Therefore, the existence of ET would seem to be more apparent to O-CSFS/MPS than CCFCF@C/MPS system. To get deep into evidence for ET, additional electrochemical analyses such as CV/LSV/i-t curves and OCP with and without adding MPS/PCM were performed [17,37,67] (Text S6).

At first, CV curves CCFCF@C/GCE and O-CSFS/GCE electrodes were scanned at 60 mV/s from − 1.4–0.6 V vs. Ag/AgCl in 0.5 M Na_2SO_4 with and without 200 mg/L MPS and 20 mg/L PCM. It is observed from Fig. S20(a, b) that CCFCF@C/GCE and O-CSFS/GCE in the electrolyte containing MPS/PCM exhibited larger CV area with higher redox peak current density than the control ones. In other words, the interfacial interaction between the electrodes and MPS/PCM took effect when MPS/PCM was introduced. The enhanced electrochemical catalytic activity of CCFCF@C/GCE and O-CSFS/GCE in the presence of MPS/PCM was mainly attributed to ET from PCM. Compared to CCFCF@C/GCE, O-CSFS/GCE displayed much larger CV area with much higher redox peak current density under the same condition (Fig. S20(c)), suggesting higher ET amount in case of O-CSFS/GCE although the occurrence of ET could be observed on the surface of both CCFCF@C/GCE and O-CSFS/GCE electrodes.

Secondly, LSV curves at 20 mV/s in 0.5 M Na_2SO_4 containing 200 mg/L MPS and 20 mg/L PCM were adopted to further support the boosted ET of O-CSFS/GCE. As can be seen from Fig. S21(a, b) that while CCFCF@C/GCE needed 2.339 V vs. Ag/AgCl to afford 10 mA/cm^2 in the absence of MPS/PCM, only 1.829 V vs. Ag/AgCl was required to reach the same current density on O-CSFS/GCE in the same electrolyte. Once MPS/PCM was added, the potential needed to afford 10 mA/cm^2 was reduced to 2.313 and 1.503 V vs. Ag/AgCl for CCFCF@C/GCE and O-CSFS/GCE, respectively. Compared to CCFCF@C/GCE, the driving potential of O-CSFS/GCE was significantly lower, 0.81 V vs. Ag/AgCl down as shown in Fig. S21(c).

Overall, the results from CV and LSV were quite consistent, partly providing evidence for the appearance of ET. However, the mechanism involving in the interaction between the coated electrodes and MPS/PCM still needs to be clarified. In this case, current response and OCP would be useful. As i-t curves in Fig. 8(a, b) show, without adding MPS/PCM, the current of CCFCF@C/GCE and O-CSFS/GCE increased and remained quite stable after 150 s, or, more precisely, no any changes in the current of the two electrodes. However, the current of the two electrodes dropped suddenly as 1 mL of 1 g/L MPS was added and rose gradually afterwards. The first decrease in the current was largely due to the migration of electrons from CCFCF@C/GCE and O-CSFS/GCE to MPS, during which electron density of CCFCF@C and O-CSFS on GCE was redistributed [68], leading to the formation of so-called surface-active CCFCF@C/MPS and O-CSFS/MPS complexes. At the same

time, MPS accepted electrons, resulting in its reduction, or rather its decomposition. These complexes became more stable as the current increased later on, implying that MPS was just decomposed partly. The succeeding addition of PCM caused the current to decrease to a larger extent, that is to say, there was the migration of electrons from PCM to the MPS via CCFCF@C and O-CSFS as electron mediators, contributing to more decomposition of MPS. This is why the current decreased more when PCM was added. The decrease in current was even enhanced as MPS or PCM with a higher concentration was added. These results could, therefore, explain the added PCM-induced enhancement in the MPS decomposition (Fig. S19). In addition, the magnitude of decrease in the current would be positively correlated to the electrons migrated. Thus, electrons mediated by O-CSFS were more than those by CCFCF@C.

The formation of such surface-active CCFCF@C/MPS and O-CSFS/MPS complexes could be corroborated by OCP measurements with the addition of MPS before or after PCM. As PCM acts as an electron donor, its addition before MPS will not combine with CCFCF@C or O-CSFS to form the complexes. If this speculation is true, changes in the potential will not be observed when PCM is added before MPS. Indeed, Fig. 8(c) shows clearly this. Whereas the addition of MPS first induced a sharp increase in the potential, the addition of PCM first in Fig. 8(d) did not increase but rather decrease the potential. The increase in the potential suggests MPS could combine with O-CSFS to form the surface-active O-CSFS/MPS complex, while PCM could not. The rise in the potential was even more obvious as increasing the MPS concentration from 1 g/L to 2 g/L at the same volume added. The addition of PCM later continued to raise the potential to a higher level and decreased afterwards, revealing that the presence of PCM made O-CSFS firstly transfer more electrons to MPS to reach the high-valent oxidation state of O-CSFS, at which the potential of O-CSFS/GCE was highest. The oxidized O-CSFS then accepted electrons from PCM, leading to a fall in the potential [67]. Similar phenomenon was also seen when MPS was added after PCM (Fig. 8(d)). At a lower concentration of PCM (100 mg/L), the added MPS could not return O-CSFS to the lower oxidation state (i.e., the potential did not decrease) as the PCM concentration was not high enough. In this case, the oxidation of PCM was just by ROS (i.e., $SO_4^{\bullet -}$ and $^1O_2$). Nevertheless, at a higher concentration of PCM (200 mg/L), the addition of MPS afterwards induced a fall in the potential, meaning that the PCM concentration was high enough to loss its electrons to O-CSFS. Briefly, the PCM degradation could be driven by ROS and ET, but ROS played a minor role in case of low PCM concentration, and did not account for the superior catalytic performance of O-CSFS. ET, on the other hand, proved to be overwhelmingly dominant, responsible for most degradation of PCM in O-CSFS/MPS system. Furthermore, the superior oxidative capacity of O-CSFS could be examined by OCP with the successive addition of MPS at different concentrations. As shown in Fig. 8(e, f), the potential increased proportionally with increasing concentration of MPS, signifying the superb sensitivity of O-CSFS, or rather its superior oxidative capacity towards MPS.

3.12. Exploring mechanisms behind MPS activation for PCM degradation

The PCM degradation in CCFCF@C/MPS and O-CSFS/MPS was well demonstrated to be driven by ROS and ET. For ROS, their participation was associated with $SO_4^{\bullet -}$ and $^1O_2$ without $^\bullet OH$ despite the presence of $^\bullet OH$ coming from MPS activation. With lower $SO_4^{\bullet -}$ generated, the superior PCM degradation in O-CSFS/MPS system could not be attributed to its higher contribution. $^1O_2$, on the other hand, was generated with the same amount in both systems, hence its limited contribution to higher PCM degradation in O-CSFS/MPS system than in CCFCF@C/MPS system. Different from ROS, ET appeared to be pathway that directly enhanced the PCM degradation by O-CSFS-activated MPS. High surface area as well as large pore volume of O-CSFS were likely to be the first factors accounting for this. However, the underlying causes could be due to the highest Co(II) content, highest ECSA, boosted interfacial redox property, greatest diffusion coefficient, most efficient kinetics behavior,
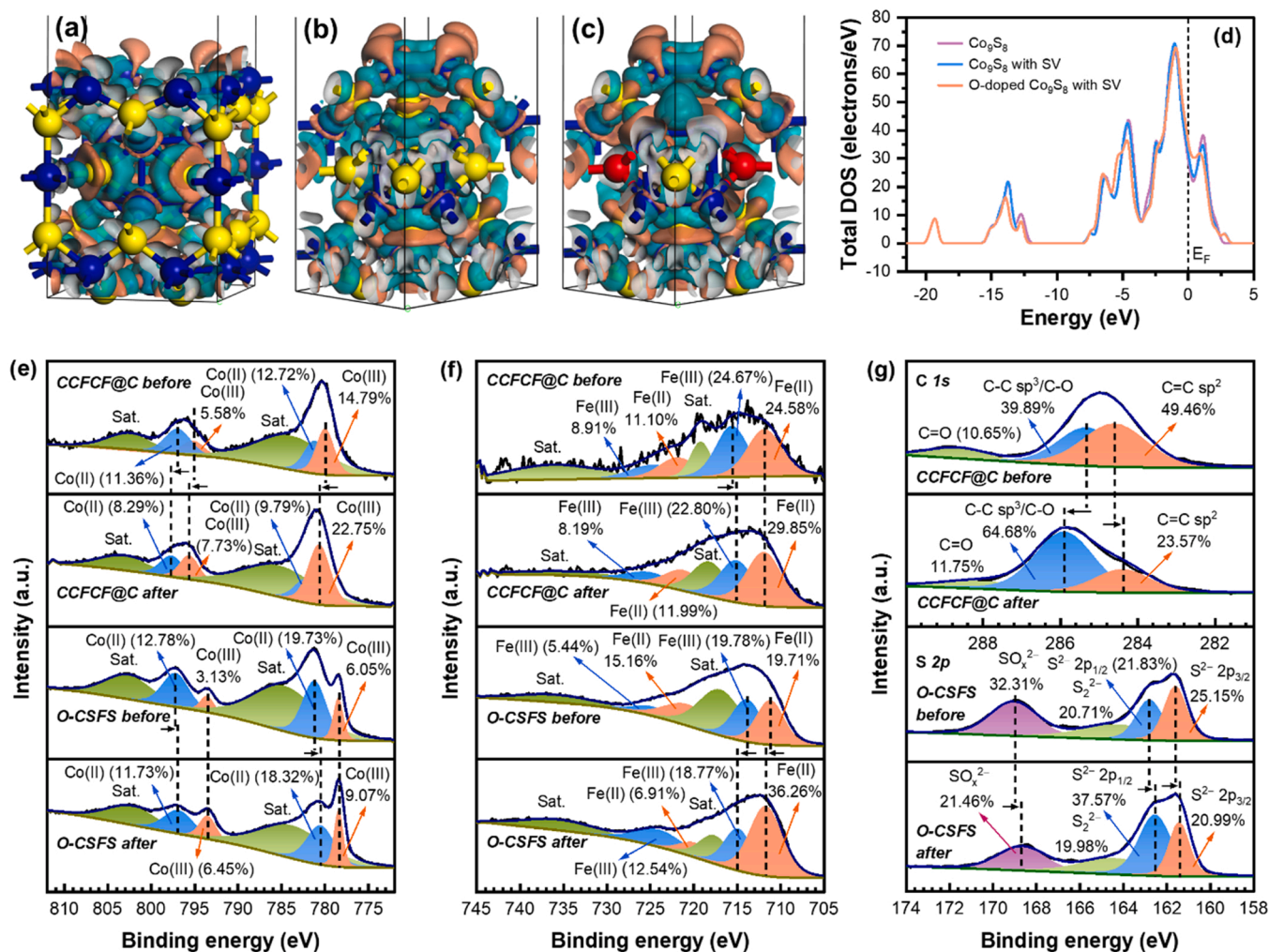
Fig. 9. (a-c) Optimized structures mapped with EDD of (a) Co_9S_8 (100), (b) Co_9S_8 (100) with SV, and (c) O-doped Co_9S_8 (100) with SV (dark blue: Co, yellow: S, red: O, turquoise: positive charge, orange: negative charge); (d) corresponding total DOS; (e-g) XPS spectra of CCFCF@C and O-CSFS before and after activation for one cycle: (e) Co *2p*, (f) Fe *2p*, and (g) C *1 s* and S *2p*.

lowest resistance, fastest ET, and lowest overpotential of O-CSFS. These features were most likely because of the benefits from SV and oxygen doping-induced high conductivity.

To verify this, theoretical simulations were first performed with the use of Co_9S_8 as an example (Text S7). The structures of Co_9S_8 (100) and (b) Co_9S_8 (100) with SV (before optimization) and the optimized structure of O-doped Co_9S_8 (100) with SV are shown in Fig. S25. The formation energy of Co_9S_8 (100) was -23230.9959 eV, lower than that of Co_9S_8 (100) with SV (-22950.13630 eV), suggesting the formation of SV on Co_9S_8 (100) required higher energy. However, combination of SV and oxygen doping reduced the formation energy of Co_9S_8 (100) to -23418.2271 eV, revealing that oxygen was easily doped to Co_9S_8 (100) with SV. Electron density differences (EDD) of these models were mapped in Fig. 9(a-c), which exhibited changes in the distribution of electrons between atoms in these models, i.e., the redistribution of surface charge was modulated after incorporation of SV and oxygen doping. The corresponding density of states (DOS) in Fig. 9(d) revealed that DOS of the original Co_9S_8 (100) near Fermi level (E_F) was weaken than that of Co_9S_8 (100) with SV, indicating that SV introduction was beneficial to the increase of conductivity. Notably, the DOS near E_F was even enhanced more after some S atoms was substituted with O atoms. These results demonstrated that the incorporation of SV and oxygen doping not only modulated the surface charge distribution, but also optimized the electronic structure by increasing the conductivity, thereby accelerating the performance towards MPS activation.

As abovementioned, the PCM degradation would be driven by two pathways. In ROS-driven pathway, MPS might be activated according to equations in Table 2, in which Eqs. (7−14, 21−40) were due to self-decomposition of MPS to generate $^\bullet OH$, $SO_4^{\bullet-}$, $SO_5^{\bullet-}$ (a weak oxidation species with low potential of 1.1 V at pH 7 [49]), $^1O_2$, and $O_2^{\bullet-}$. In contrast, metal species-activated MPS made the others occur. In addition, Eqs. (21−23) also occurred on account of Eq. (19). After generation via Eqs. (17, 18), $SO_4^{\bullet-}$ continued to be disproportionated via Eq. (24) and reduced by OH^- via Eq. (25) to form $^\bullet OH$. Finally, it was self-quenched via Eq. (26). The generation of $S_2O_8^{2-}$ via Eqs. (23, 26) could also quench $SO_4^{\bullet-}$ Eq. (27). As generated via Eqs. (15, 16), $^\bullet OH$ tended to combine together via Eq. (35) at a rate constant of 5.5×10^9 L mol^{-1} s^{-1} to form H_2O_2, which could continue to react back with $^\bullet OH$ to form $O_2^{\bullet-}$ via Eq. (36). Right after appearance, $O_2^{\bullet-}$ could make Eqs. (37, 38) possible by dissociation or reaction with H^+ to form $^1O_2$. $^\bullet OH$ from Eqs. (15, 16) and $O_2^{\bullet-}$ from Eq. (36) could react together to form $^1O_2$ via Eq. (39). Ultimately, this pathway could be terminated by the formation of $^\bullet OH$ via Eq. (40) as H_2O_2 from Eqs. (35, 37, 38) can react with $O_2^{\bullet-}$ from Eq. (36). Overall, these equations occurred consecutively to form different ROS, contributing marginally to PCM degradation. Through these equations, it seems likely that the participation of metal species should be taken into account as they almost governed all the reactions of activating MPS in ROS-driven pathway as indicated above. Changes in their oxidation states between before and after reactions are, therefore, necessary to compare. In Fig. 9(e, f), these changes in relative
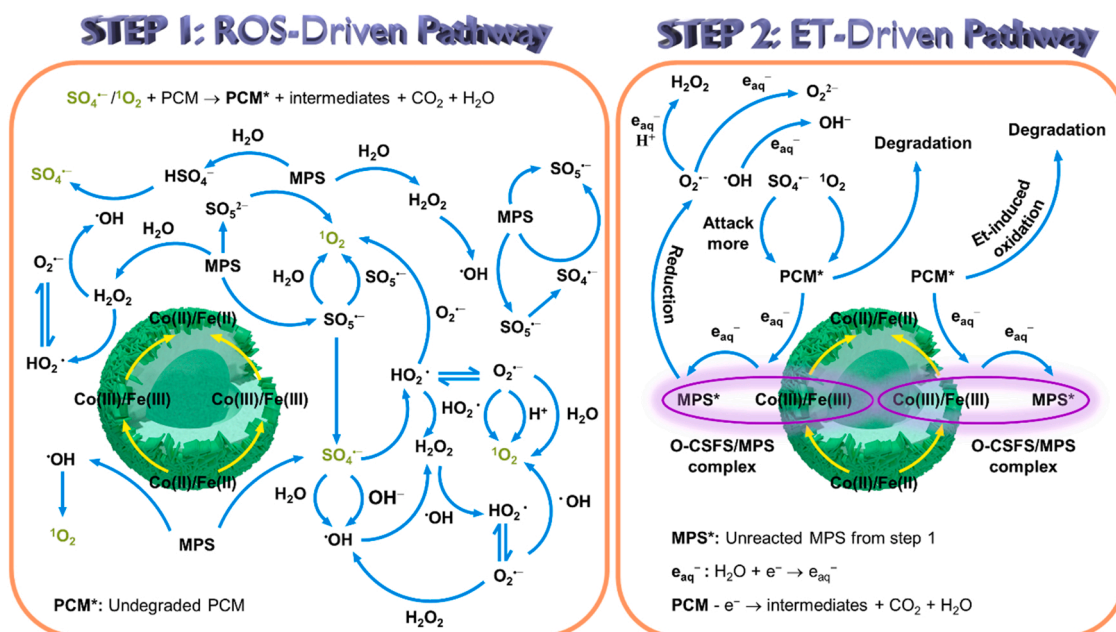
Fig. 10. (a) Schematic illustration of MPS activation over O-CSFS for PCM degradation.

percentage as well as binding energy of Co and Fe were easy to observe. For Co $2p$, most of Co species in CCFCF@C shifted to higher binding energy after reaction, while Co(II) in O-CSFS showed the contrary, suggesting there was differences in electron density of Co species between these catalysts. Situating at lower binding energy is positively correlated to higher defect content, i.e., the number of metal species in the unbound state is higher, or rather higher electron density, hence higher electron density of Co species in O-CSFS. Regarding percentage, both CCFCF@C and O-CSFS had higher Co(III) and lower Co(II) after reaction, manifesting Eqs. (19, 20, 42, 45) occurred slowly. As to Fe $2p$, the peak position of Fe(III) in CCFCF@C was moved to lower binding energy. Meanwhile, most of peak position of Fe species in O-CSFS showed upwards. These suggests Fe $2p$ in CCFCF@C had higher electron density than that in O-CSFS after reaction. The difference in electron density also reveals that Fe actually participated in the reaction. However, the increase in Fe(II) and decrease in Fe(III) percentage of both CCFCF@C and O-CSFS after reaction implies that Eqs. (43, 44) and Eq. (46) for O-CSFS preferred to take place.

In ET-driven pathway, electrons appeared as a result of carbon matrix in case of CCFCF@C, and electrons-rich sites on the surface O-CSFS (i.e., the sites around SV). Further, Co or Fe in CoFe alloy could also deemed as electron-rich sites of CCFCF@C as these two atoms of CoFe alloy are both in the low oxidation state. Because $CoFe_2O_4$ was one of the components of CCFCF@C, OV also deserves consideration in this case. Anyway, these electrons were first donated by CCFCF@C and O-CSFS to reduce MPS to a certain extent via Eqs. (47−64, 76) for both CCFCF@C and O-CSFS and Eqs. (65−75) for O-CSFS as listed in Table 3, after which unreacted MPS tended to combine with CCFCF@C and O-CSFS to form surface-active CCFCF@C/MPS and O-CSFS/MPS complexes. Subsequently, these complexes with high reduction potential as revealed by OCP above acquired electrons from PCM, resulting in PCM oxidation and simultaneously reduction of those active sites in CCFCF@C and O-CSFS (Eqs. (63, 64)) that were in high oxidation state after MPS activation in the first step. Right after accepting electrons from PCM, these sites came back to electrons-rich sites and thereby continuing to donate electrons to MPS for further MPS reduction, i.e., enhanced MPS decomposition. That is why MPS was decomposed faster in the presence of PCM (Fig. S19). By this way, CCFCF@C and O-CSFS played as electron mediators, transferring electrons from PCM to MPS to accelerate MPS activation. The accelerated MPS activation, therefore, would contribute

to higher ROS generation. However, the fact remains that MPS activated over CCFCF@C but not over O-CSFS enhanced ROS generation (Fig. 6(f, g)) in the presence of PCM. The decrease in ROS generation by PCM in O-CSFS/MPS system could be due to (i) the consumption of ROS by PCM and (ii) the reaction of ROS with electrons via Eqs. (49, 50, 56, 57, 59). However, the later could not explain the decline of $^1O_2$ generation in O-CSFS/MPS/PCM system. On that account, the consumption of $^1O_2$ by PCM was likely the underlying cause. Moreover, the quenching effect of electrons on $O_2^{\bullet-}$ via Eqs. (49, 50) could not be ignored in considering the reason for $O_2^{\bullet-}$ to be absent in both CCFCF@C/MPS and O-CSFS/MPS systems.

With the presence of C matrix, the performance of CCFCF@C could be enhanced as π electron-rich sp^2-hybridized C (C=C) could activate MPS via Eqs. (54, 55) and all the relevant reactions (Eqs. (47−53, 56−64, 76)). On the other hand, O-CSFS had several S species, whose participation in the reactions could be seen via Eqs. (45, 46, 65−75). To confirm this, changes in C percentage before and after reaction were first compared together as shown in Fig. 9(g). Accordingly, the relative content of both C=O and C-C sp^3/C-O increased, while that of C=C sp^2 decreased after reaction, indicating undeniable role of C species in the reaction. Different from C $1s$, S $2p$ in O-CSFS tended to acquire electrons from PCM to form other S species, and simultaneously oxidize PCM. These species then could react together or with Co(III)/Fe(III) to form different ROS, enhancing PCM degradation. As Fig. 9(g) shows, S species had higher electron density after reaction, mainly because of the accumulated electrons from PCM. Moreover, the relative content of these species was also found to change, especially S^{2-} and SO_4^{2-}. While S^{2-} increased, SO_4^{2-} decreased after reaction, suggesting Eq. (65) might occur to form S^{2-}. The formation of S^{2-} could account for its increase after reaction. At the same time, SO_4^{2-} was consumed, resulting in the decline of SO_4^{2-} after reaction. In addition, S^{2-} could react directly with MPS by accepting electrons from PCM via Eq. (68) to form SO_3^{2-} and SO_4^{2-}, but SO_4^{2-} decreased after reaction. Thus, this equation might occur slowly than Eq. (65). After formation via Eq. (65), S^{2-} could react with ether Co(III) or Fe(III) via Eqs. (66, 67) to regenerate Co(II), Fe(II), and S_2^{2-}. However, Co(II) decreased after reaction, preventing Eq. (66) from occurring. Meanwhile, Fe(II) increased, reflecting the possibility of Eq. (67), but the slight decrease in S_2^{2-} made this equation occur slowly. Briefly, S species in O-CSFS served as an electron acceptor, acquiring electrons form PCM, resulting in PCM oxidation. Also, the formation of
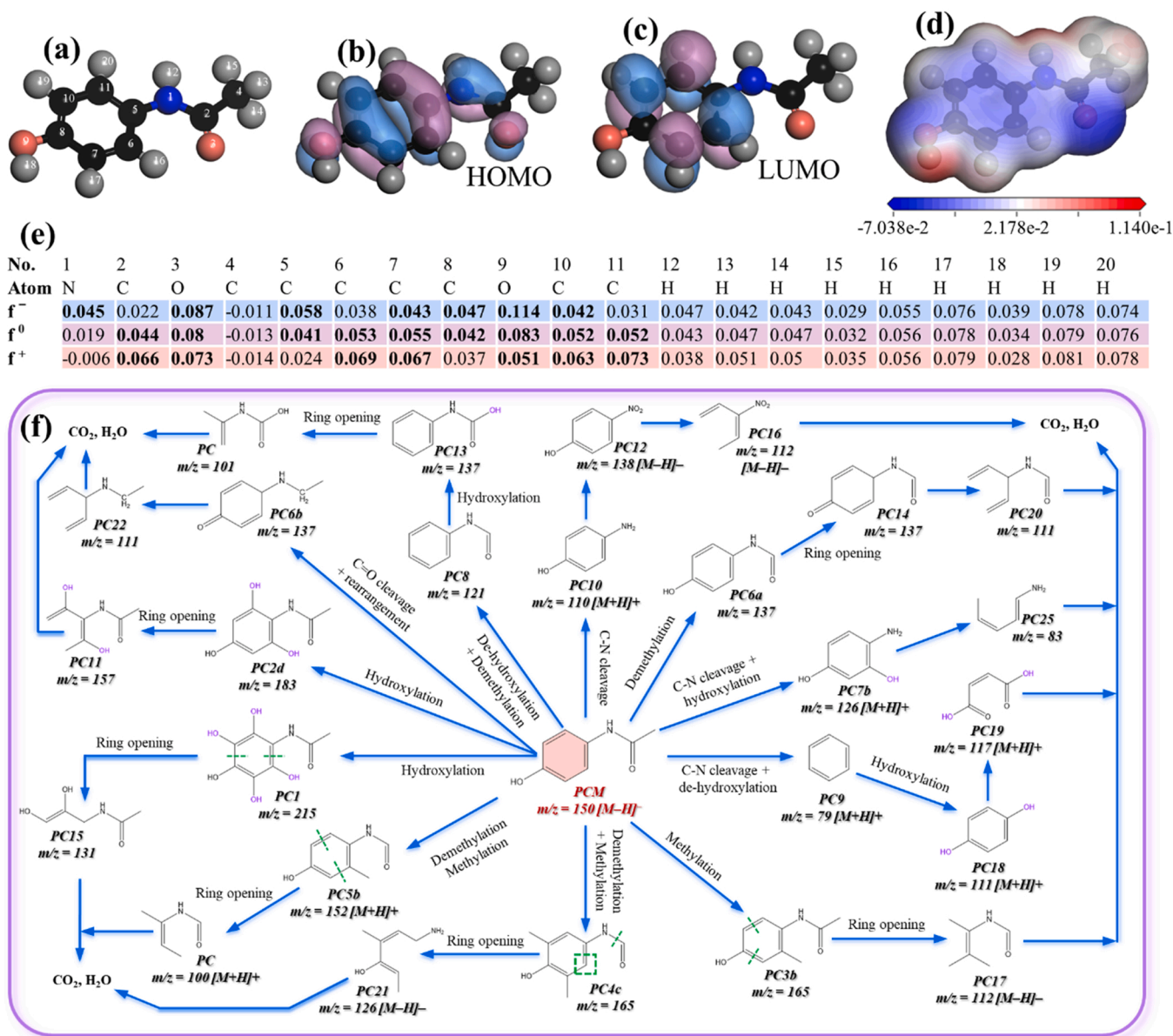
Fig. 11. (a-e) DFT calculation for PCM: (a) the optimized molecule structure, (b) HOMO, (c) LUMO, (d) ESP (isovalue = 0.017), (e) condensed Fukui index distribution for electrophilic attack (f^-), radical attack (f^0), and nucleophilic attack (f^+); and (f) degradation pathways of PCM in O-CSFS/MPS system.

S^{2-} through this way contributed to regeneration of Fe(II), thereby further enhancing the performance of O-CSFS. Also, $S_2O_8^{2-}$, which could be formed from $SO_5^{\bullet-}$ via Eq. (23) or from $SO_4^{\bullet-}$ via Eq. (26), can be transformed into $SO_4^{\bullet-}$ via Eq. (76) by electrons from PCM and C matrix and Co/Fe atoms around OV for CCFCF@C and around SV for O-CSFS. Therefore, the presence of electrons could regenerate $SO_4^{\bullet-}$ and maintain the efficient PCM degradation.

Finally, the role of oxygen species could be revealed via the relative content between before and after reaction in Fig. S26. The increase in OL suggests the possible occurrence of Eq. (60), after which Co(III) and Fe (III) could be reduced to Co(II) and Fe(II) via Eqs. (61, 62). However, OL increased, hence the exclusion of these two equations. Meanwhile, OV (for CCFCF@C) was consumed, implying its involvement in the reaction. As reported in the previous study [37], unpaired electrons around OV could capture either O in O-O bond of MPS to result in $SO_4^{\bullet-}$ or $^{\bullet}OH$ via Eqs. (54, 55). Thus, the occurrence of these two equations, could explain the consumption of OV. Furthermore, the presence of electrons in Eqs. (47, 60) could be also considered as the reason for OV to be decrease after reaction. Similarly, OH/SO_x^{2-} of O-CSFS also decreased, from

71.31% to 48.14%. The decrease of OH/SO_x^{2-} was quite consistent with the consumption of SO_x^{2-} in S *2p*, proving that O-doping caused SO_x^{2-} to appear, thereby improving the performance of O-CSFS via ET-driven nonradical degradation pathway of PCM. In contrast, OA increased, largely due to the surface adsorption of H_2O [37].

In summary, the mechanism for PCM degradation can be illustrated in Fig. 10. Accordingly, the degradation of PCM was driven by two pathways, including ROS and ET. In the first pathway, MPS was activated partly over O-CSFS to form $SO_4^{\bullet-}/^{\bullet}OH$ and $^1O_2$ through different ways. Subsequently, $SO_4^{\bullet-}$ and $^1O_2$ contributed directly to PCM degradation, causing PCM to degrade to some extent. In the second pathway, undegraded PCM donated its electrons to Co(III)/Fe(III) of the surface-active O-CSFS/MPS complex as well as to S^{2-} and $SO_4^{\bullet-}$ species of S *2p* in O-CSFS. By this way, PCM was oxidized. At the same time, electrons from PCM mediated by O-CSFS would continue to reduce unreacted MPS to form $SO_4^{\bullet-}$ and $^1O_2$ for further attacking PCM, resulting in its efficient degradation.

3.13. Explicating pathways of PCM degradation

The highest occupied molecular orbital (HOMO), the lowest unoccupied molecular orbital (LUMO), electrostatic potential (ESP), and condensed Fukui indexes would be useful to explore reaction sites of PCM [3,17,37,69] (see method in Text S7). The optimized structure of PCM is displayed in Fig. 11(a) and its HOMO, LUMO, and ESP are mapped in Fig. 11(b, c, d), while the Fukui indexes are presented in Fig. 11(e). The HOMO of PCM mainly distributes around N1, O3, C5, C7, C8, O9, and C10, making these sites easily lose electrons, and can be attacked by electrophiles, such as $^1O_2$ and the surface-active O-CSFS/MPS complex. Meanwhile, the LUMO is related to electron-poor sites. Thus C6, C7, C10, and C11 are readily to be attacked by nucleophiles, like OH^-. It is observed that the sites covered by HOMO and LUMO are quite similar to those with high f^- and f^+, respectively, confirming the above sites have high electrophilic and nucleophilic activities. In contrast, C2, C6, C7, C10, and C11 highlighted by white in Fig. 11(d) are found to have high f^0, so they are vulnerable to radical attacks, such as $SO_4^{\bullet-}$. In addition, O3, C5, C7, C8, O9, C10, and C11 with high f^0 can also receive further attacks from $SO_4^{\bullet-}$. Based on the most vulnerable sites above and LCQ-LC/MS analysis in Fig. S27, the PCM degradation can be subject into various reactions, such as hydroxylation, methylation, demethylation + methylation, demethylation, C=O cleavage + rearrangement, C-N cleavage + hydroxylation, de-hydroxylation + demethylation, C-N cleavage + dihydroxylation, and C-N cleavage to form different primary intermediates. For hydroxylation, except PC1, four other intermediates PC2a-PC2d might be formed (Table S5). However, PC2d had the lowest total energy of − 18108.079351 eV, enabling its formation easiest. Similarly, PC3b, PC4c, PC5b, and PC7b were formed preferentially. These primary intermediates along with PC6a, PC6b, PC8, PC9, and PC10 continued to be attacked at the active sites shown in Fig. S28-S42, forming other small molecules and being mineralized into CO_2 and H_2O after ring opening. Whole pathways were illustrated in Fig. 11(f) and all related intermediates were listed in Table S6.

4. Conclusions

Herein, bimetal sulfides (O-CSFS) with a well-defined structure and hollow configuration were successfully fabricated via mono-step sulfidation of nanocube-assembled hollow bimetallic cobalt-iron Prussian blue analogue (CoFePBA) nanospheres-derived hollow Fe-doped cobalt oxide (Fe-Co_3O_4). The as-prepared O-CSFS exhibited distinct and superior physicochemical properties, enabling it to show outstanding catalytic activity for MPS activation to degrade PPCPs, PCM. In particularly, O-CSFS was found to accelerate the decomposition of MPS much faster than CCFCF@C-x as well as its precursor (Fe-Co_3O_4), mostly due to more electroactive sites and lower charge transfer resistance that were resulted from SV and oxygen doping-induced high conductivity. Moreover, the presence of SV and doped oxygen made O-CSFS possess more active sites, boosting the performance through the formation of surface-active O-CSFS/MPS complex. This complex tended to deprive electrons from PCM, leading to the oxidation of PCM, or rather, the PCM degradation via ET-driven nonradical degradation pathway. These results demonstrated that O-CSFS served as a promising and superior heterogeneous catalyst for activating MPS to degrade PPCPs.

CRediT authorship contribution statement

Ta Cong Khiem: Data curation, Writing – original draft. **Eilhann Kwon:** Data curation, preparation of figures. **Stanisław Wacławek:** Data curation. **Nguyen Nhat Huy:** Data curation, Visualization, Investigation. **Yu-Chih Tsai:** Data curation. **Jorge Bedia:** Data curation, Visualization, Investigation. **Xiaoguang Duan:** Writing – review & editing. **Afshin Ebrahimi:** Writing – review & editing. **Farshid Ghanbari:** Writing – original draft. **Kun-Yi Andrew Lin:** Writing – original draft.

Declaration of Competing Interest

The authors declare that they have no known competing financial interests or personal relationships that could have appeared to influence the work reported in this paper.

Data Availability

The authors are unable or have chosen not to specify which data has been used.

Appendix A. Supporting information

Supplementary data associated with this article can be found in the online version at doi:10.1016/j.apcatb.2023.122550.

References

[1] Y. Chen, J. Vymazal, T. Březinová, M. Koželuh, L. Kule, J. Huang, Z. Chen, Occurrence, removal and environmental risk assessment of pharmaceuticals and personal care products in rural wastewater treatment wetlands, Sci. Total Environ. 566 (2016) 1660–1669.

[2] W.-J. Liu, E. Kwon, N.N. Huy, T.C. Khiem, G. Lisak, T. Wi-Afedzi, C.-C. Wu, F. Ghanbari, K.-Y.A. Lin, Facilely-prepared sulfide-doped Co3O4 nanocomposite as a boosted catalyst for activating Oxone to degrade a sunscreen agent, J. Taiwan Inst. Chem. Eng. 133 (2022), 104253.

[3] P.-H. Mao, T.C. Khiem, E. Kwon, H.-C. Chang, H.M. Bui, X. Duan, H. Yang, S. Ghotekar, W.-H. Chen, Y.-C. Tsai, Ambient-Visible-Light-Mediated Enhanced Degradation of UV Stabilizer Bis (4-hydroxyphenyl) methanone by Nanosheet-Assembled Cobalt Titanium Oxide: A Comparative and DFT-Assisted Investigation, Water 14 (2022) 3318.

[4] D.D. Tuan, E. Kwon, S. Phattarapattamawong, B.X. Thanh, T.C. Khiem, G. Lisak, H. Wang, K.-Y.A. Lin, Nitrogen-containing carbon hollow nanocube-confined cobalt nanoparticle as a magnetic and efficient catalyst for activating monopersulfate to degrade a UV filter in water, J. Environ. Chem. Eng. 10 (2022), 106989.

[5] J.-Y. Yin, E. Kwon, B.X. Thanh, G. Lisak, W. Da, Oh, K.-Y.A. Lin, Cobalt sulfide nanosheets derived from sulfurization of Prussian blue analogue as an enhanced catalyst for activating monopersulfate to degrade caffeine, J. Taiwan Inst. Chem. Eng. 123 (2021) 115–123.

[6] F. Ghanbari, A. Yaghoot-Nezhad, S. Wacławek, K.-Y.A. Lin, J. Rodríguez-Chueca, F. Mehdipour, Comparative investigation of acetaminophen degradation in aqueous solution by UV/Chlorine and UV/H2O2 processes: kinetics and toxicity assessment, process feasibility and products identification, Chemosphere 285 (2021), 131455.

[7] M.R.K. Kashani, R. Kiani, A. Hassani, A. Kadier, S. Madihi-Bidgoli, K.-Y.A. Lin, F. Ghanbari, Electro-peroxone application for ciprofloxacin degradation in aqueous solution using sacrificial iron anode: a new hybrid process, Sep. Purif. Technol. 292 (2022) 121026.

[8] B. Palanivel, C. Hu, M. Shkir, S. AlFaify, F.A. Ibrahim, M.S. Hamdy, A. Mani, Fluorine doped g-C3N4 coupled NiFe2O4 heterojunction: consumption of H2O2 for production of hydroxyl radicals towards paracetamol degradation, Colloid and Interface Science, Communications 42 (2021), 100410.

[9] F. Ghanbari, S. Giannakis, K.-Y.A. Lin, J. Wu, S. Madihi-Bidgoli, Acetaminophen degradation by a synergistic peracetic acid/UVC-LED/Fe (II) advanced oxidation process: Kinetic assessment, process feasibility and mechanistic considerations, Chemosphere 263 (2021), 128119.

[10] S. Giannakis, K.-Y.A. Lin, F. Ghanbari, A review of the recent advances on the treatment of industrial wastewaters by Sulfate Radical-based Advanced Oxidation Processes (SR-AOPs), Chem. Eng. J. 406 (2021), 127083.

[11] P. Hu, H. Su, Z. Chen, C. Yu, Q. Li, B. Zhou, P.J. Alvarez, M. Long, Selective degradation of organic pollutants using an efficient metal-free catalyst derived from carbonized polypyrrole via peroxymonosulfate activation, Environ. Sci. Technol. 51 (2017) 11288–11296.

[12] M. Nie, Y. Deng, S. Nie, C. Yan, M. Ding, W. Dong, Y. Dai, Y. Zhang, Simultaneous removal of bisphenol A and phosphate from water by peroxymonosulfate combined with calcium hydroxide, Chem. Eng. J. 369 (2019) 35–45.

[13] W. Ren, G. Nie, P. Zhou, H. Zhang, X. Duan, S. Wang, The intrinsic nature of persulfate activation and N-doping in carbocatalysis, Environ. Sci. Technol. 54 (2020) 6438–6447.

[14] P. Shao, S. Yu, X. Duan, L. Yang, H. Shi, L. Ding, J. Tian, L. Yang, X. Luo, S. Wang, Potential difference driving electron transfer via defective carbon nanotubes toward selective oxidation of organic micropollutants, Environ. Sci. Technol. 54 (2020) 8464–8472.

[15] W.-J. Liu, E. Kwon, B.X. Thanh, T.C. Khiem, G. Lisak, J. Lee, K.-Y.A. Lin, 3D hexagonal hierachitectured cobalt sulfide as an enhanced catalyst for activating monopersulfate to degrade sunscreen agent ensulizole, J. Taiwan Inst. Chem. Eng. 131 (2022), 104109.

[16] W.-J. Liu, H. Yang, Y.-K. Park, E. Kwon, C.-W. Huang, B.X. Thanh, T.C. Khiem, S. You, F. Ghanbari, K.-Y.A. Lin, Enhanced degradation of ultra-violet stabilizer Bis (4-hydroxy) benzophenone using oxone catalyzed by hexagonal nanoplate-assembled CoS 3-dimensional cluster, Chemosphere 288 (2022), 132427.

[17] T.C. Khiem, X. Duan, W.-J. Liu, Y.-K. Park, H.M. Bui, W.-D. Oh, S. Ghotekar, Y. F. Tsang, K.-Y.A. Lin, MOF-templated Hollow Cobalt Sulfide as an Enhanced Oxone Activator for Degradation of UV Absorber: Key Role of Sulfur Vacancy-Induced Highly Active CoII Sites, Chem. Eng. J. (2022), 139699.

[18] Y. Zhao, Z. Shi, H. Li, C.-A. Wang, Designing pinecone-like and hierarchical manganese cobalt sulfides for advanced supercapacitor electrodes, J. Mater. Chem. A 6 (2018) 12782–12793.

[19] Y. Li, T. Chen, S. Zhao, P. Wu, Y. Chong, A. Li, Y. Zhao, G. Chen, X. Jin, Y. Qiu, Engineering cobalt oxide with coexisting cobalt defects and oxygen vacancies for enhanced catalytic oxidation of toluene, ACS, Catalysis 12 (2022) 4906–4917.

[20] Q. Gao, W. Luo, X. Ma, Z. Ma, S. Li, F. Gou, W. Shen, Y. Jiang, R. He, M. Li, Electronic modulation and vacancy engineering of Ni9S8 to synergistically boost efficient water splitting: Active vacancy-metal pairs, Appl. Catal. B: Environ. 310 (2022), 121356.

[21] X. Li, S. Zhao, G. Qu, X. Wang, P. Hou, G. Zhao, X. Xu, Defect engineering in Co-doped Ni3S2 nanosheets as cathode for high-performance aqueous zinc ion battery, J. Mater. Sci. Technol. 118 (2022) 190–198.

[22] B. Qiu, Y. Zhang, X. Guo, Y. Ma, M. Du, J. Fan, Y. Zhu, Z. Zeng, Y. Chai, Nitrogen-induced interfacial electronic structure of NiS 2/CoS 2 with optimized water and hydrogen binding abilities for efficient alkaline hydrogen evolution electrocatalysis, J. Mater. Chem. A 10 (2022) 719–725.

[23] K. Zhang, Y. Duan, N. Graham, W. Yu, Unveiling the synergy of polymorph heterointerface and sulfur vacancy in NiS/Ni3S2 electrocatalyst to promote alkaline hydrogen evolution reaction, Appl. Catal. B: Environ. (2022), 122144.

[24] L. Zhang, Q. Zhou, J. Liang, L. Yue, T. Li, Y. Luo, Q. Liu, N. Li, B. Tang, F. Gong, Enhancing electrocatalytic NO Reduction to NH3 by the CoS nanosheet with sulfur vacancies, Inorg. Chem. (2022).

[25] D. Li, L. Zhao, Q. Xia, J. Wang, X. Liu, H. Xu, S. Chou, Activating MoS2 nanoflakes via sulfur defect engineering wrapped on CNTs for stable and efficient Li-O2 batteries, Adv. Funct. Mater. 32 (2022) 2108153.

[26] Z. Wang, X. Liao, M. Zhou, F. Huang, K.A. Owusu, J. Li, Z. Lin, Q. Sun, X. Hong, C. Sun, Interfacial and Vacancies Engineering of Copper Nickel Sulfide for Enhanced Oxygen Reduction and Alcohols Oxidation Activity, Energy & Environmental Materials.

[27] J. Lin, P. Wang, H. Wang, C. Li, X. Si, J. Qi, J. Cao, Z. Zhong, W. Fei, J. Feng, Defect-rich heterogeneous MoS2/NiS2 nanosheets electrocatalysts for efficient overall water splitting, Advanced, Science 6 (2019) 1900246.

[28] D. Balaji, J. Madhavan, M. Preeyanghaa, M. Hussien, M. Selvaraj, S. Murugesan, B. Neppolian, Phosphorus co-doped reduced graphene oxide embedded flower-like CoS/CoS2 heterostructure as an efficient electrocatalyst for hydrogen evolution reaction in acidic media, J. Alloy. Compd. 907 (2022), 164506.

[29] H. Huang, A. Liu, Q. Kang, X. Ye, H. Chen, W.-N. Su, T. Ma, Synthesis of one-dimensional vanadium-doped CoS/Co9S8 heterojunctions as bifunctional electrocatalysts for zinc-air battery, Mater. Today Energy 25 (2022), 100968.

[30] S.-C. Wang, D. Xiong, C. Chen, M. Gu, F.-Y. Yi, The controlled fabrication of hierarchical CoS2@ NiS2 core-shell nanocubes by utilizing prussian blue analogue for enhanced capacitive energy storage performance, J. Power Sources 450 (2020), 227712.

[31] Z. Zhang, Y. Huang, X. Liu, C. Chen, Z. Xu, P. Liu, Zeolitic imidazolate frameworks derived ZnS/Co3S4 composite nanoparticles doping on polyhedral carbon framework for efficient lithium/sodium storage anode materials, Carbon 157 (2020) 244–254.

[32] H. Xu, Y. Sheng, New insights into the degradation of chloramphenicol and fluoroquinolone antibiotics by peroxymonosulfate activated with FeS: Performance and mechanism, Chem. Eng. J. 414 (2021), 128823.

[33] X. Liu, H. Li, S. Gao, Z. Bai, J. Tian, Peroxymonosulfate activation by different iron sulfides for bisphenol-A degradation: Performance and mechanism, Sep. Purif. Technol. 289 (2022), 120751.

[34] J. Liu, X. Deng, S. Zhu, N. Zhao, J. Sha, L. Ma, F. He, Porous oxygen-doped NiCoP nanoneedles for high performance hybrid supercapacitor, Electrochim. Acta 368 (2021) 137528.

[35] Y. Li, Q. Guo, Y. Jiang, W. Shen, M. Li, R. He, A novel ball-in-ball hollow oxygen-incorporating cobalt sulfide spheres as high-efficient electrocatalyst for oxygen evolution reaction, Chin. Chem. Lett. 32 (2021) 755–760.

[36] Q. Wu, Y. Zhu, J. Guo, S. Wang, X. Feng, Z. Chen, Insight into the influence of doped oxygen on active sites of molybdenum sulfide materials in hydrogen evolution reaction, Int. J. Hydrog. Energy 46 (2021) 11721–11730.

[37] T.C. Khiem, D.D. Tuan, E. Kwon, N.N. Huy, W.-D. Oh, W.-H. Chen, K.-Y.A. Lin, Degradation of dihydroxybenzophenone through monopersulfate activation over nanostructured cobalt ferrites with various morphologies: A comparative study, Chem. Eng. J. 450 (2022), 137798.

[38] L.E. Caldeira, C.S. Erhardt, F.R. Mariosi, J. Venturini, R.Y.S. Zampiva, O.R. K. Montedo, S. Arcaro, C.P. Bergmann, S.R. Bragança, Correlation of synthesis parameters to the structural and magnetic properties of spinel cobalt ferrites (CoFe2O4)–an experimental and statistical study, J. Magn. Magn. Mater. 550 (2022), 169128.

[39] Y. Lei, L. Zhang, D. Zhou, C. Xiong, Y. Zhao, W. Chen, X. Xiang, H. Shang, B. Zhang, Construction of interconnected NiO/CoFe alloy nanosheets for overall water splitting, Renew. Energy (2022).

[40] J. Mujtaba, L. He, H. Zhu, Z. Xiao, G. Huang, A.A. Solovev, Y. Mei, Co9S8 nanoparticles for hydrogen evolution, ACS Appl. Nano Mater. 4 (2021) 1776–1785.

[41] N. Cheng, X. Chen, L. Zhang, Z. Liu, Reduced graphene oxide doping flower-like Fe7S8 nanosheets for high performance potassium ion storage, J. Energy Chem. 54 (2021) 604–611.

[42] Y. Huang, A. Xie, F. Seidi, W. Zhu, H. Li, S. Yin, X. Xu, H. Xiao, Core-shell heterostructured nanofibers consisting of Fe7S8 nanoparticles embedded into S-doped carbon nanoshells for superior electromagnetic wave absorption, Chem. Eng. J. 423 (2021), 130307.

[43] Y. Deng, X. Wang, Z. Wang, X. Wang, Z. Li, L. Wang, C. Zhou, D. Chen, Y. Luo, Yolk–shell structured nickel cobalt sulfide and carbon nanotube composite for high-performance hybrid supercapacitors, Energy Fuels 35 (2021) 5342–5351.

[44] S.H. Yang, G.D. Park, J.K. Kim, Y.C. Kang, New strategy to synthesize optimal cobalt diselenide@ hollow mesoporous carbon nanospheres for highly efficient hydrogen evolution reaction, Chem. Eng. J. 424 (2021), 130341.

[45] X. Liu, Z. Yin, M. Cui, L. Gao, A. Liu, W.-N. Su, S. Chen, T. Ma, Y. Li, Double shelled hollow CoS2@ MoS2@ NiS2 polyhedron as advanced trifunctional electrocatalyst for zinc-air battery and self-powered overall water splitting, J. Colloid Interface Sci. 610 (2022) 653–662.

[46] F. Shi, K. Zhu, X. Li, E. Wang, X. Zhu, W. Yang, Porous carbon layers wrapped CoFe alloy for ultrastable Zn-Air batteries exceeding 20,000 charging-discharging cycles, J. Energy Chem. 61 (2021) 327–335.

[47] Y. Wu, P. Deng, Y. Tian, J. Feng, J. Xiao, J. Li, J. Liu, G. Li, Q. He, Simultaneous and sensitive determination of ascorbic acid, dopamine and uric acid via an electrochemical sensor based on PVP-graphene composite, J. Nanobiotechnol. 18 (2020) 1–13.

[48] P. Pauletto, S. Lütke, G. Dotto, N. Salau, Forecasting the multicomponent adsorption of nimesulide and paracetamol through artificial neural network, Chem. Eng. J. 412 (2021), 127527.

[49] P. Neta, R.E. Huie, A.B. Ross, Rate constants for reactions of inorganic radicals in aqueous solution, J. Phys. Chem. Ref. Data 17 (1988) 1027–1284.

[50] H.-H. Chen, Y.-K. Park, E. Kwon, Y.F. Tsang, B.X. Thanh, T.C. Khiem, S. You, C. Hu, K.-Y.A. Lin, Nanoneedle-Assembled Copper/Cobalt sulfides on nickel foam as an enhanced 3D hierarchical catalyst to activate monopersulfate for Rhodamine b degradation, J. Colloid Interface Sci. 613 (2022) 168–181.

[51] H.E. Gsponer, C.M. Previtali, N.A. García, Kinetics of the photosensitized oxidation of polychlorophenols in alkaline aqueous solution, Toxicol. Environ. Chem. 16 (1987) 23–37.

[52] S. Zhu, X. Li, J. Kang, X. Duan, S. Wang, Persulfate activation on crystallographic manganese oxides: mechanism of singlet oxygen evolution for nonradical selective degradation of aqueous contaminants, Environ. Sci. Technol. 53 (2018) 307–315.

[53] Y. Zhao, L. Yu, C. Song, Z. Chen, F. Meng, M. Song, Selective Degradation of Electron-Rich Organic Pollutants Induced by CuO@ Biochar: The Key Role of Outer-Sphere Interaction and Singlet Oxygen, Environmental Science & Technology, (2022).

[54] K.Z. Huang, H. Zhang, Direct electron-transfer-based peroxymonosulfate activation by iron-doped manganese oxide (δ-MnO2) and the development of galvanic oxidation processes (GOPs), Environ. Sci. Technol. 53 (2019) 12610–12620.

[55] A. Li, Z. Wu, T. Wang, S. Hou, B. Huang, X. Kong, X. Li, Y. Guan, R. Qiu, J. Fang, Kinetics and mechanisms of the degradation of PPCPs by zero-valent iron (Fe°) activated peroxydisulfate (PDS) system in groundwater, J. Hazard. Mater. 357 (2018) 207–216.

[56] E.-T. Yun, J.H. Lee, J. Kim, H.-D. Park, J. Lee, Identifying the nonradical mechanism in the peroxymonosulfate activation process: singlet oxygenation versus mediated electron transfer, Environ. Sci. Technol. 52 (2018) 7032–7042.

[57] B.H. Bielski, G.G. Shiue, S. Bajuk, Reduction of nitro blue tetrazolium by CO2-and O2-radicals, J. Phys. Chem. 84 (1980) 830–833.

[58] M.E. Lindsey, M.A. Tarr, Quantitation of hydroxyl radical during Fenton oxidation following a single addition of iron and peroxide, Chemosphere 41 (2000) 409–417.

[59] P. Neta, V. Madhavan, H. Zemel, R.W. Fessenden, Rate constants and mechanism of reaction of sulfate radical anion with aromatic compounds, J. Am. Chem. Soc. 99 (1977) 163–164.

[60] J. Criquet, N.K.V. Leitner, Reaction pathway of the degradation of the p-hydroxybenzoic acid by sulfate radical generated by ionizing radiations, Radiat. Phys. Chem. 106 (2015) 307–314.

[61] Y. Zong, X. Guan, J. Xu, Y. Feng, Y. Mao, L. Xu, H. Chu, D. Wu, Unraveling the overlooked involvement of high-valent cobalt-oxo species generated from the cobalt (II)-activated peroxymonosulfate process, Environ. Sci. Technol. 54 (2020) 16231–16239.

[62] J. Jiang, Z. Zhao, J. Gao, T. Li, M. Li, D. Zhou, S. Dong, Nitrogen vacancy-modulated peroxymonosulfate nonradical activation for organic contaminant removal via high-valent cobalt-oxo species, Environ. Sci. Technol. 56 (2022) 5611–5619.

[63] Z. Wang, J. Jiang, S. Pang, Y. Zhou, C. Guan, Y. Gao, J. Li, Y. Yang, W. Qiu, C. Jiang, Is sulfate radical really generated from peroxydisulfate activated by iron (II) for environmental decontamination? Environ. Sci. Technol. 52 (2018) 11276–11284.

[64] Y. Bao, W.-D. Oh, T.-T. Lim, R. Wang, R.D. Webster, X. Hu, Elucidation of stoichiometric efficiency, radical generation and transformation pathway during catalytic oxidation of sulfamethoxazole via peroxymonosulfate activation, Water Res. 151 (2019) 64–74.

[65] Q. Yi, J. Ji, B. Shen, C. Dong, J. Liu, J. Zhang, M. Xing, Singlet oxygen triggered by superoxide radicals in a molybdenum cocatalytic Fenton reaction with enhanced REDOX activity in the environment, Environ. Sci. Technol. 53 (2019) 9725–9733.

[66] R.E. Huie, C.L. Clifton, Temperature dependence of the rate constants for reactions of the sulfate radical, SO4-, with anions, J. Phys. Chem. 94 (1990) 8561–8567.

[67] M.-M. Wang, L.-J. Liu, J.-T. Wen, Y. Ding, J.-R. Xi, J.-C. Li, F.-Z. Lu, W.-K. Wang, J. Xu, Multimetallic CuCoNi oxide nanowires in situ grown on a nickel foam substrate catalyze persulfate activation via mediating electron transfer, Environ. Sci. Technol. 56 (2022) 12613–12624.

[68] L. Yang, Z. Xiong, J. Li, Z. Wu, X. Zhao, C. Zhao, Y. Zhou, Y. Qian, B. Lai, Iron active sites encapsulated in N-doped graphite for efficiently selective degradation of emerging contaminants via peroxymonosulfate (PMS) activation: Inherent roles of adsorption and electron-transfer dominated nonradical mechanisms, Chem. Eng. J. 444 (2022), 136623.

[69] T.C. Khiem, P.-H. Mao, Y.-K. Park, X. Duan, B.X. Thanh, C. Hu, S. Ghotekar, Y. F. Tsang, K.-Y.A. Lin, Templating agent-mediated Cobalt oxide encapsulated in Mesoporous silica as an efficient oxone activator for elimination of toxic anionic azo dye in water: mechanistic and DFT-assisted investigations, Chemosphere (2022), 137309.